

### Technical Articles

- Microstructure based Continuum Creep Model and its Applicability to the Long-term Creep Behaviour of Ferritic-Martensitic Steels
- Pressure Induced Phase Transformations and Thermal Expansion of Energetic Material TEX

### Young Officer's Forum

- Study on the Kinetics of the Catalytic Generation of Uranous for Spent Fuel Reprocessing

### Young Researcher's Forum

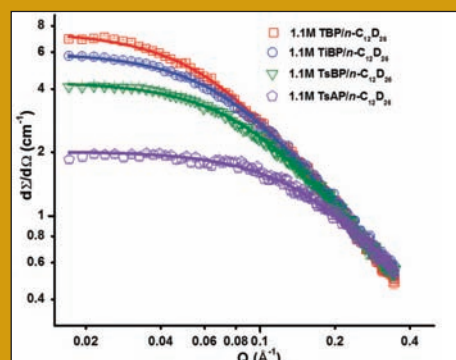
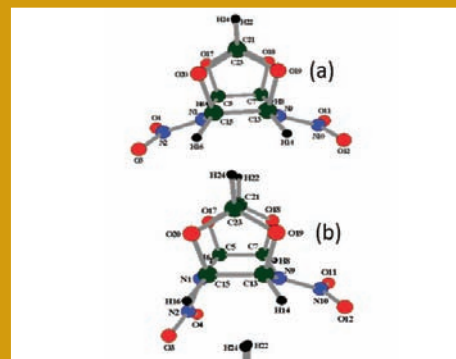
- Trends in Small Angle Neutron Scattering of Actinide – Trialkyl Phosphate Complexes: A Molecular insight into Third Phase Formation

### Conference and Meeting Highlights

- International Conference on Nanostructuring by Ion Beams (ICNIB-2019)
- 4<sup>th</sup> National Conference URJAVARAN – 2019

### HBNI-IGCAR Corner

### Awards & Honours



## *From the Editorial Committee*

### *Dear Reader*

It is our pleasant privilege to forward a copy of the latest issue of IGC Newsletter (Volume 123, January 2020 issue).

In the first technical article, Dr. J. Christopher and colleagues, Metallurgy and Materials Group has discussed about the “Microstructure based Continuum Creep Model and its Applicability to the Long-term Creep Behaviour of ferritic-martensitic steels”.

In the second technical article, Dr. T. R. Ravindran, Material Science Group has discussed about the “Pressure Induced Phase Transformations and Thermal Expansion of Energetic Material TEX”.

Shri S. Ramakrishna Reddy, Reprocessing Group has described about the “Study on the Kinetics of the Catalytic Generation of Uranous for Spent Fuel Reprocessing” in the Young Officer’s Forum.

This issue’s Young Researcher’s Forum features an article by Dr. Aditi Chandrasekar, Materials Chemistry & Metal Fuel Cycle Group, IGCAR discussing about the “Trends in Small Angle Neutron Scattering of Actinide – Trialkyl Phosphate Complexes: A Molecular insight into Third Phase Formation”.

We are happy to share with you the awards, honours and distinctions earned by our colleagues.

We look forward to your comments, continued guidance and support.

With best wishes and personal regards

Editorial Committee, IGC Newsletter

## New Year Message

### Dear Colleagues,

I wish you and your families a very joyous, pleasant, healthy and fulfilling New Year. This is the time of the year to look back at the achievements of IGCAR and GSO in 2019 and set our goals towards greater accomplishments in 2020.

It is a matter of pride that our Centre celebrated its Foundation Day for the first time on 30<sup>th</sup> April 2019, coinciding with the commemoration of the birth centenary of Dr. Vikram Sarabhai. It was indeed our privilege that this occasion was graced by Dr. R. Chidambaram, former Chairman AEC, Shri K. N. Vyas, Secretary DAE & Chairman AEC, as also many former Directors and Group Directors. We also had the privilege of family members of many of the colleagues visiting IGCAR. We will be continuing celebrating the Foundation Day annually.

In 2019, Fast Breeder Test Reactor, the flagship experimental reactor of our Centre attained 32 MWt during the 27<sup>th</sup> and 28<sup>th</sup> irradiation campaigns. The turbo generator was also synchronized to grid delivering an electrical output of about 7 MWe. The 29<sup>th</sup> irradiation campaign at 32 MWt power has also commenced. Necessary regulatory approvals have been sought to raise the FBTR power to its rated full power level of 40 MWt. Design of critical components and analyses of vital plant dynamic parameters have been completed. Various equipments like supplementary control panel, seismic instrumentation, global sodium ionisation detection system for detecting sodium leaks, mobile purification circuit for sodium purification in manual flooding tanks have been successfully commissioned. Operational life of FBTR has been re-assessed and towards extending life of grid plate, replacement of axial steel shielding in fuel subassemblies with tungsten carbide has been recommended. Towards this, high-density tungsten carbide pellets have been synthesised using spark plasma sintering technique for incorporation into carbide fuel sub-assemblies.

The unique U-233 based Kalpakkam Mini Reactor (KAMINI) continued to operate up to 30 kWt for neutron radiography of boron coated gamma compensated ion chambers, vanadium self powered neutron detectors, fission chambers from ECIL and PFBR neutron detector. Seismic analysis of reactor vessel with



beam tubes and irradiation of boron carbide, T9 and D9 alloys with AS-466, ammonium chloride, europium with tungsten standard and nickel foam with nickel and manganese standards, gold foil samples, thermo-luminescent dosimeter pellet by neutron activation analysis was taken up.

Prototype Fast Breeder Reactor (PFBR) is in an advanced stage of commissioning and IGCAR continues to provide all necessary technical support towards obtaining safety clearances. The first batch of 42 fuel sub-assemblies for PFBR has been shifted from Interim Fuel Storage building to BHAVINI site.

CORAL (Compact Reprocessing facility for Advanced Fuels in Lead cells) facility has realized its designated reprocessing mandate of 14 spent fuel sub assemblies over 48 campaigns. Eight more reprocessing campaigns have been completed at CORAL after relicensing by AERB. Demonstration Fuel Reprocessing Plant (DFRP) is in the second stage of commissioning with the commencement of acid-TBP runs with the qualification of leak testing of all plutonium handling containment systems.

As part of continuing endeavor towards development of metallic fuel, 1000 kg LiCl-KCl eutectic salt for electro-refining of uranium has been prepared. Oxidation conditions for U-Pu-Zr metal fuels for aqueous processing has been optimized. We have forayed into production of radiopharmaceutical <sup>89</sup>Sr (bone palliative) by establishing chemical and biological purity control. An ion mobility mass spectrometer for explosive detection has been developed and field trials have been completed.

Significant experimental facilities like measuring the contact angle of sodium, cavity-ring down spectrometer facility for the precise detection of trace level impurities in cover gas mixture, facility for functional testing and qualification of large diameter bearing under simulated operating conditions have been commissioned. Facilities for fabrication of U-Pu-Zr metal fuel by injection casting method and pyro-processing studies of uranium and its alloys have also been commissioned.

In our endeavor for development of improved materials and process for FBRs, improved Alloy D9I, 316LN+ SS, B-added 9Cr-1Mo steel including welding consumables, efficient alternate process for hard-facing of PFBR components have been developed. Under-sodium three-dimensional ultrasonic imaging at 180°C has been demonstrated and plasma nitriding of a mock-up case ring of PFBR secondary sodium pump, has been carried out. A novel high-performance nanophase-modified fly-ash concrete with inhibitor has shown promise for extending the life span of concrete structures of nuclear installations. A new 500W average power Nd-YAG Laser system capable of cutting through up to 15 mm thick stainless steel tube, has been successfully interfaced with a hot-cell for remote operations. A turbine rotor for Advanced Ultra-Supercritical Coal fired Thermal power plant, involving dissimilar metal welding has been successfully welded and qualified. Design and development of plutonium continuous air monitor (PuCAM), development of airborne Time Domain Electromagnetic (TDEM) system for exploration of atomic minerals, indigenous design & development of numerical protection relays, development of indigenous wireless sensor network to enhance avalanche forecasting capability and indigenous simulator platform for FBRs are some of the other notable achievements.

The construction activities for the Fast Reactor Fuel Cycle Facility (FRFCF) continue to make steady progress. A single uninterrupted concrete pour of size 8200 Cu.m. of temperature controlled concrete was taken up in FRP block 4 and successfully completed within 130 hours against an estimated time of 145 hours. This is the single largest pour ever done in DAE and has surpassed the earlier FRFCF/DAE record. Training Centre of FRFCF, the first-ever green building in DAE, obtained Gold rated Green Building Certificate from Indian Green Building Council (IGB).

We are happy that twenty three young trained scientists and engineers (OCES-2018, 13<sup>th</sup> Batch) have successfully completed their orientation programme at BARC Training School at IGCAR and were placed in various units of DAE. The programmes of HBNI continue to progress with full vigour. The principals, teachers and staff as also students and their parents of the 2 Kendriya Vidyalayas and 3 Atomic Energy Central Schools deserve our

compliments for continuing improved performances of students in the X & XII Board Examinations.

GSO continues to build residential buildings for employees and also strives towards enhancing the infrastructural facilities and greenery in both the townships. The security isolation fencing in both the townships have been completed and restricted entry to all sectors of the townships have been put in place to ensure security and safety of all residents. Hospital continues to provide excellent health care to the residents of the townships. The efforts put in by employees of GSO in maintaining the townships serene and clean is commendable.

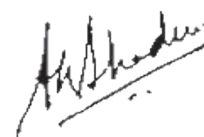
These achievements would have been impossible but for the tireless and painstaking efforts put in by all colleagues of IGCAR and GSO. I take this opportunity to thank staff association in IGCAR and GSO for their whole hearted cooperation in all these endeavor.

The year ahead has a number of challenges in various domains. Foremost being raising the FBTR power beyond 32 MWt and the technical support towards commissioning of PFBR, followed by fabrication of sodium bonded metal fuel pins and subassemblies, pilot plant production of Sr-89, commissioning of pyro-processing R&D facility for electro-refining in 10 kg scale for U/U-alloys and DFRP for regular reprocessing of FBTR fuel, establishment of neutron calibration facility, refurbishment of FBTR & KAMINI for continued uninterrupted operation, design conceptualization of future FBRs and Metal Fuel Test Reactor (FBTR-2), development of pre service and in-service inspection system for FBRs, development of improved imaging and inspection techniques for advanced NDE and enhancement of radiological safety are some of our immediate priorities.

The Administration, Accounts and Auxiliary Departments of IGCAR and GSO have continued to provide commendable services guiding and supporting the execution of the programmes.

I look forward for your continued support, cooperation and dedicated efforts, towards marching ahead to the next level of excellence.

I once again wish you successes in all your endeavors in the year ahead.



(Dr. Arun Kumar Bhaduri)

## Microstructure based Continuum Creep Model and its Applicability to the Long-term Creep Behaviour of Ferritic-Martensitic Steels

The ferritic-martensitic steels containing 9% Chromium are favoured structural materials for steam generator applications in power plants. The creep strength of the steel is derived from (i) solute strengthening due to the presence of molybdenum/tungsten in the matrix, (ii) dislocation strengthening arising from the initial high dislocation density of the order of  $1 \times 10^{14} \text{ m}^{-2}$ , (iii) boundary hardening from fine lath/subgrains and (iv) precipitation strengthening from finely distributed  $\text{M}_{23}\text{C}_6$  and MX type (niobium/vanadium carbide/carbonitride) precipitates. Creep strength of 9% Cr steels breaks down in the long-term creep regime due to the recovery of subgrains caused by coarsening of  $\text{M}_{23}\text{C}_6$  precipitates and the conversion of finely distributed useful MX precipitates and consequent formation and growth of complex nitride Z-phase i.e. Cr(V,Nb)N precipitates. In common, Z-phase grows very rapidly at the expense of MX precipitates. These observations strongly indicate that evolution of microstructural features (softening of subgrains accompanied with the decrease in dislocation density and the variations in the number density of different precipitates) influence the creep behaviour of 9% Cr steels and these variables need to be incorporated into the kinetic rate relationships for the development of constitutive models. In general, understanding and modelling of creep behaviour of 9% Cr steels are important for safe life design and remnant life assessment of components operating at high temperatures. The continual improvement in understanding of underlying microstructure variables in 9% Cr steels has led to the development of new constitutive models or modification in existing models. In this regard, microstructure based continuum creep damage model and its applicability for the plain 9Cr-1Mo and modified 9Cr-1Mo steel have been presented.

### Experimental Data for Modelling

For modelling creep behaviour of plain 9Cr-1Mo steel, the experimental creep strain ( $\epsilon$ )-time ( $t$ ) data obtained on P9 steel in quenched and tempered (Q+T) condition has been used in the present analysis. The chemical composition of the steel (in wt.%) is as follows: Fe-0.1C-9.27Cr-1.05Mo-0.63Mn-0.75Si-0.001S-0.02P with 190 ppm of nitrogen. In order to implement the model to describe the long-term creep behaviour of modified 9Cr-1Mo steel, the creep data (NIMS data) obtained for the steel up to the

rupture lifetime  $\sim 10^5$  h have been used in this investigation.

### Modelling Framework and Optimization Methodology

The microstructure based kinetic creep law for the description of creep deformation and damage behaviour of 9% Cr steels is given as

$$\dot{\epsilon} = \dot{\epsilon}_0 \frac{D_d}{1 - \left(1 - \frac{c_e}{c_0}\right) D_s} \sinh \left[ \frac{\sigma (1-H)}{\sigma_0 (1-D_C)(1-D_p)} \right] \quad (1)$$

where  $\dot{\epsilon}$  is the creep rate,  $\dot{\epsilon}_0$  is the characteristic strain rate,  $D_d$  defines the damage parameter related to the variations in dislocation density with time,  $D_s$  is damage parameter for the solute depletion from the matrix,  $c_0$  and  $c_e$  are solute concentrations at  $t = 0$  and at equilibrium in matrix, respectively,  $D_C$  is the damage parameter associated with the cavitation damage,  $D_p$  defines the damage parameter associated with the precipitate coarsening,  $\sigma$  is the applied stress,  $H$  is the normalised kinematic back stress and  $\sigma_0$  is the normalising stress related to the dislocation-particle interaction. The above kinetic creep law i.e. Equation (1) was coupled with the simultaneous first-order differential equations defining the evolution of dislocation density, solute depletion, precipitate coarsening, cavitation damage and kinematic back stress for simulating the complete creep-strain time trajectory for a given applied stress. The material constants associated with the model were optimized numerically by fitting the experimental data with predicted creep strain-time data. In order to obtain the optimum values of material constants, an iterative methodology has been invoked. The iteration procedure consists of numerical integration of differential equations followed by the estimation of least-square error. Numerical integration of set of differential equations has been performed by fourth-order Runge-Kutta method. The fitting procedure was considered as a converged one when the least-square error values computed in two successive iterations are small enough than the tolerance value of  $1 \times 10^{-6}$ . The derived values of constants at the end of iterations were treated as the optimised values of material constants.

### Applicability of the Model

The experimental creep strain-time along with predicted creep

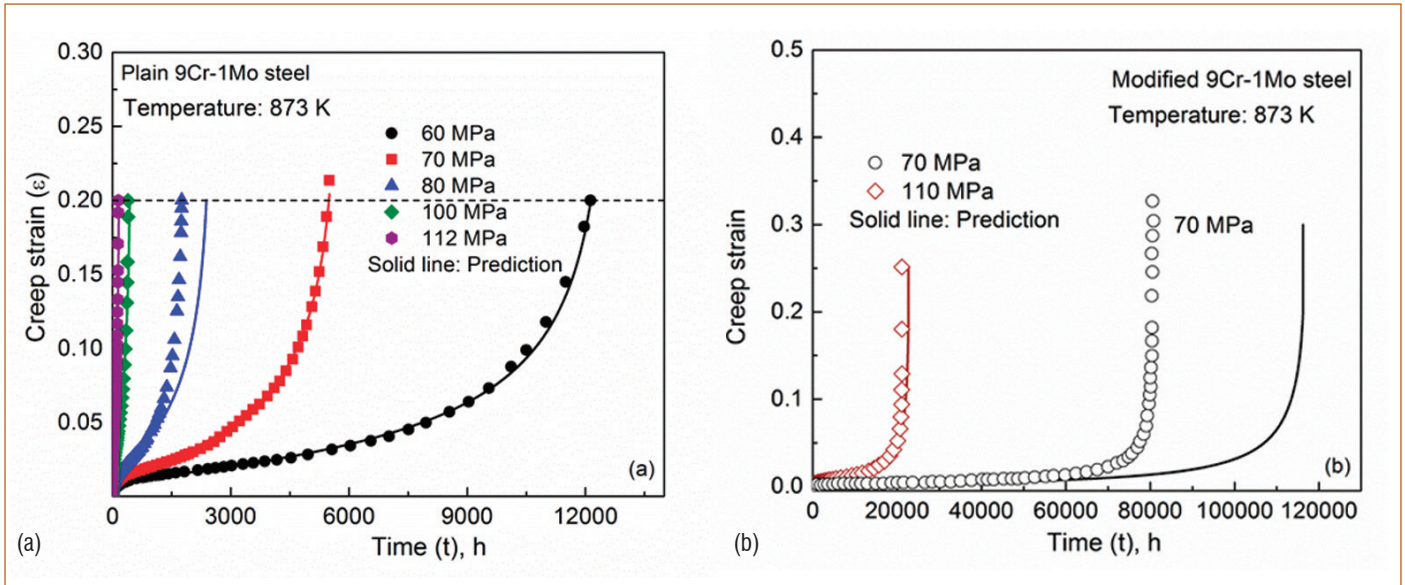


Figure 1: Experimental and predicted creep strain-time data for (a) Plain 9Cr-1Mo steel and (b) modified 9Cr-1Mo steel for different stress levels at 873 K.

strain-time data has been shown in Figure 1(a) and (b) for plain 9Cr-1Mo and modified 9Cr-1Mo steels, respectively. From Figure 1, it is discernible that the microstructure based model is appropriately applicable for the description of the creep behaviour of plain 9Cr-1Mo for both low and high stress levels. Though the model is applicable for the description of creep behaviour of modified 9Cr-1Mo steel at high stress level of 110 MPa, the predicted creep strain does not follow the experimental data at low stress level of 70 MPa. Since the model does not account for the decreasing number density of useful MX precipitates with time, it overestimates the creep rupture lifetimes at low stress

levels. Therefore, it becomes necessary to incorporate the evolution kinetics of individual precipitates during deformation for the better prediction of creep behaviour of modified 9Cr-1Mo steel in both short and long-term creep regimes.

### Further Modification in Model for Simulating Long-Term Creep Behaviour

The normalising stress  $\sigma_0$  related to dislocation-particle interaction in Equation (1) accounts for the broad variations in inter-particle spacing with strain/time but does not account for the influence of individual precipitates in both short and long-term

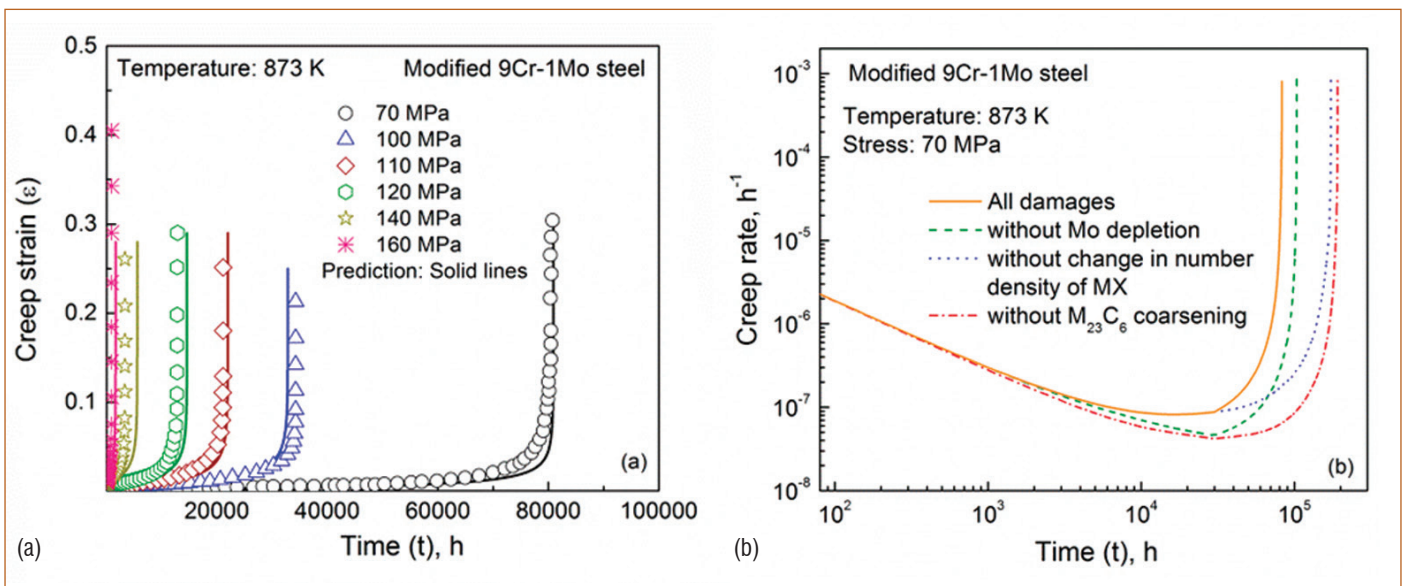


Figure 2. (a) Experimental and predicted creep strain-time data for modified 9Cr-1Mo steel for different stress levels at 873 K and (b) influence of individual precipitates on creep behaviour of the steel for the stress level of 70 MPa at 873 K.

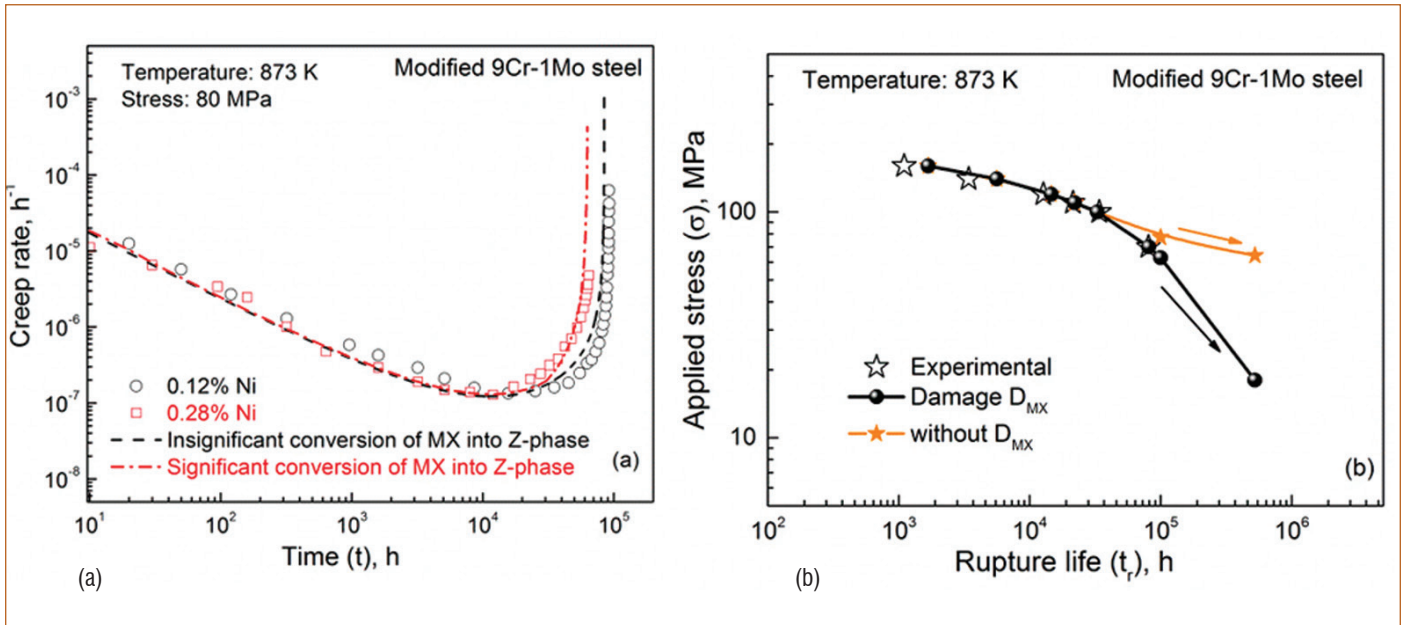


Figure 3. (a) Comparison between predicted and experimental creep rate-time data for 80 MPa at 873 K for the heats containing 0.12 and 0.28% Ni, respectively and (b) Applied stress vs. rupture lifetime data with and without inclusion of  $D_{MX}$ .

creep regimes. In order to account for the influence of individual precipitates on creep damage behaviour of materials,  $\sigma_0$  can be evaluated as

$$\sigma_0 = \chi_{0,i} \sum (1 + D_N^j)^{1/3} (N_i^j)^{1/3} \ln \left( \frac{\sum (1 + D_N^j) N_i^j (d_i^j / (1 - D_p^j))}{2b \sum N_i^j (1 + D_N^j)} \right) \quad (2)$$

where  $\sigma_0$  is a constant,  $N_i^j$  and  $d_i^j$  are initial number density and size of precipitates, respectively. The damage parameters  $D_p^j$  and  $D_N^j$  define damage due to particle coarsening and change in number density of precipitates, respectively. In the present analysis, the exponential function representing the rapid decrease in the number density of MX has been used and it is represented as

$$\frac{N_t^{MX}}{N_i^{MX}} = \exp [-k_f (t - t_{MX})] \quad (3)$$

where  $k_f$  is a rate constant and  $t_{MX}$  is the time beyond which appreciable change in the number density of MX particles occurs. Following the modifications, the model describe the creep strain-time data of modified 9Cr-1Mo steel for all the stress levels as shown in Figure 2(a). Moreover, the model can be used to visualise the influence of individual precipitates on the long-term creep behaviour of the 9% Cr steels as shown by Figure 2(b) as an example for the applied stress level of 70 MPa at 873 K. The decrease in number density of MX and  $M_{23}C_6$  precipitates

significantly affect the tertiary creep behaviour of the steel.

For further validating the developed model, two different conditions, one with constant initial number density of MX and another with the variations in the number density of MX, have been simulated for the stress level of 80 MPa at 873 K. It can be seen that the simulated creep rate-time data closely follows the experimental data for two different heats having varying nickel content (Figure 3(a)). It has been reported that the increasing nickel content greatly influences the long-term creep behaviour in terms of decrease in the creep-rupture strength of modified 9Cr-1Mo steel. Moreover, the model can be used to extrapolate the creep rupture lifetimes of steel for various microstructural conditions. Figure 3(b) is an example for the influence of  $D_{MX}$  on creep rupture lifetime of the steel. The above findings clearly indicate that the developed model can be successfully used for prediction of long-term creep lifetimes. The present investigation also suggests that the computer simulation of creep curves is possible for 9% Cr steels by coupling precipitation kinetics obtained from thermodynamic-kinetic data.

*Reported by  
J. Christopher and colleagues  
Metallurgy and Materials Group*

## Pressure Induced Phase Transformations and Thermal Expansion of Energetic Material TEX

Energetic materials can be classified into explosives, propellants, and pyrotechnics. Under appropriate stimuli such as impact, heat, and shock, explosives release hundreds of kilojoules of energy per mole in a short time of micro to nano seconds. The category of materials known as primary explosives are more sensitive to external stimuli and generate a short and strong shock wave on initiation whereas secondary explosives need a strong stimulus in the form of a shock wave from a primary explosive to detonate. Detonation process generates high pressures and temperatures of the order of 40 GPa and 5000 K, resulting in phase transformations including decomposition of the parent phase. The physics and chemistry of shockwaves leading to explosive reactions and the sensitivity of explosives are extensively explored and have been hot areas of research. Mechanical energy is known to be conveyed to low energy intermolecular vibrations and thereafter transferred to high energy internal modes through multiphonon up-pumping processes. Low energy lattice phonons ( $<200\text{ cm}^{-1}$ ; 25 meV) consist of translations and librations of molecules that in turn transmit shock wave energy via intermediate energy 'doorway modes' to chemical bonds, breaking them and starting violent exothermic reactions. The number of doorway modes shows a linear correlation to the impact sensitivities derived from drop hammer tests. Raman spectroscopy can probe phonons and molecular vibrations, thereby providing an in-depth understanding of energy transfer mechanisms.

Secondary explosives are generally organic molecular solids that are highly compressible and can undergo polymorphic phase transformations. In energetic materials many properties such as chemical reactivity, thermal stability, crystal density and sensitivity depend on the structure. Hence it is necessary to map the phase diagram of explosive materials at high pressures and temperatures to evaluate their performance and safety aspects. Structural and chemical stabilities of the various phases are necessary to understand the reactive behavior of explosive materials in the high pressure and temperature range that is relevant to shock wave initiation. The key requirements in the development of explosives are high performance, high thermal stability, and insensitivity toward external stimuli. CL-20 ( $\text{C}_6\text{H}_6\text{N}_{12}\text{O}_{12}$ ) and TEX ( $\text{C}_6\text{H}_6\text{N}_4\text{O}_8$ ) are two prominent and powerful secondary explosives. TEX structure is obtained by replacing four nitramine groups in CL-20 by ether bridges. However, the synthesis procedures for the two materials are different.

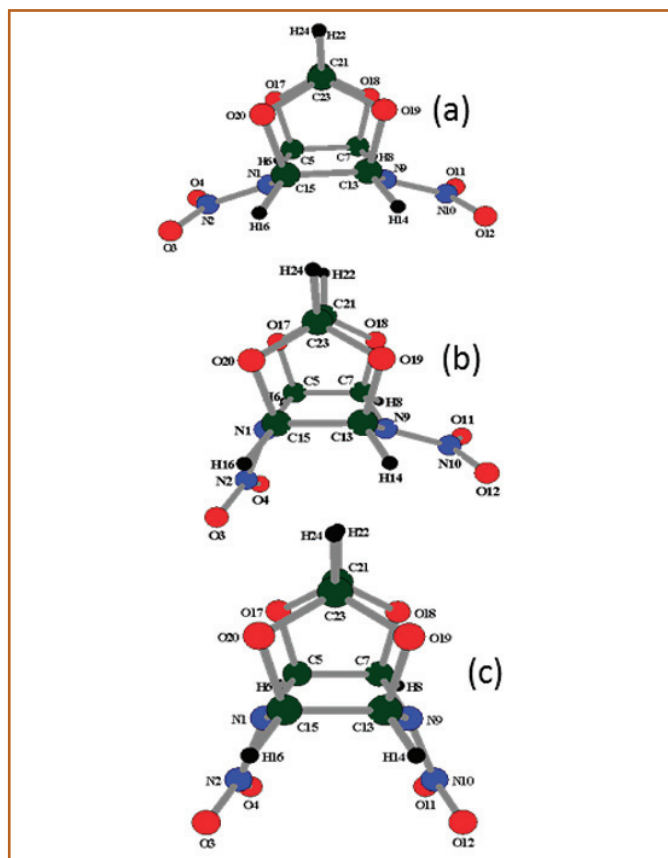


Figure 1. Molecular structures of TEX (a) exo-exo, (b) exo-endo and (c) endo-endo configurations.

The reduction in the number of sterically demanding nitramine groups reduces the sensitivity of TEX and the cage structure preserves the high density of CL-20. CL-20 can exist in four different polymorphic forms at ambient pressure and temperature, viz.,  $\alpha$ ,  $\beta$ ,  $\gamma$ ,  $\epsilon$ , the last one being thermodynamically the most stable. Whereas the phase diagram and stability of CL-20 have been determined up to 623 K and 14 GPa, there were no reports of different phases of TEX, nor any experimental reports of its high pressure behaviour. A DFT study of pressure effects on TEX suggests a structural phase transition at 61-62 GPa, but without change in symmetry ( $p\bar{1}$ ). We present direct experimental evidence for different high pressure phases of TEX.

An important property of explosives is the volume thermal expansion coefficient ( $\alpha_v$ ) that plays a significant role in applications like modeling the response of energetic material to external stimuli. In the manufacturing process, knowledge of  $\alpha_v$  gives a good understanding of the reliability and safety of devices containing explosives. A major problem in the fabrication, use

and storage of explosive components is their anisotropic thermal expansion, leading to anisotropic and irreversible shape change of the explosive crystal. Anisotropic thermal expansion in explosive crystals causes internal stress and when the effect of this stress is larger than the cohesive energy, micro cracks will appear in the crystal. These internal micro voids can induce hot spots and increase the sensitivity of the energetic materials. We have carried out temperature dependent X-ray diffraction (XRD) measurements on TEX up to 150°C and obtained the volume thermal expansion coefficient  $\alpha_v$  and its anisotropy.

TEX was synthesized from aqueous NaOH, glyoxal, formamide and other ingredients using standard procedures. TEX is a white solid crystalline particulate material. Phase identification was carried out by powder XRD technique. In-situ high pressure Raman spectra were recorded up to 27 GPa from a symmetric diamond anvil cell (DAC), using a micro Raman spectrometer with 514 nm laser excitation. High pressure XRD measurements were carried out at beam line BL-11 of Indus-2 synchrotron with monochromatic X-rays of wavelength 1.0153 Å in an angle dispersive mode in a DAC.

In order to obtain molecular vibrational frequencies we performed ab-initio calculations using the Gaussian 09W program. Structure optimizations and frequency calculations were performed by using the B3LYP hybrid functional with the aug-cc-pvtz basis set, denoted as B3LYP/aug-cc-pvtz. To obtain the phonon modes of solid TEX, structure optimization of the crystal structure was carried out with CASTEP code using Materials Studio Version 6.0 package with norm-conserving pseudo potentials and a plane wave expansion of the wave functions.

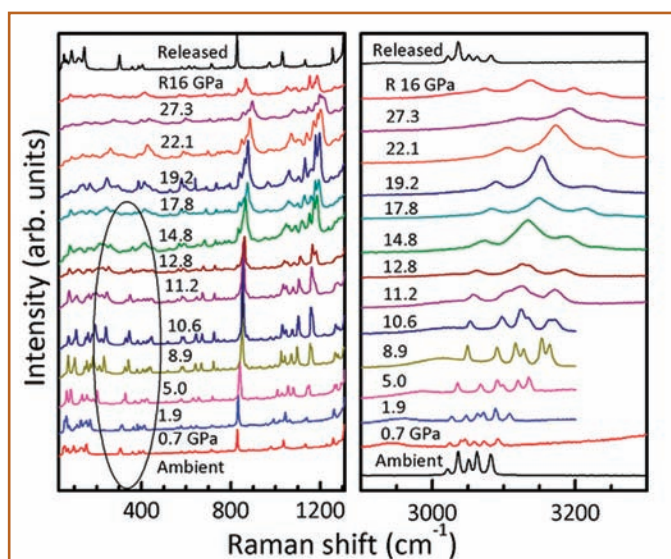


Figure 2. Raman spectra of TEX at different pressures. Ellipse denotes region of the out of plane N-N bending modes.

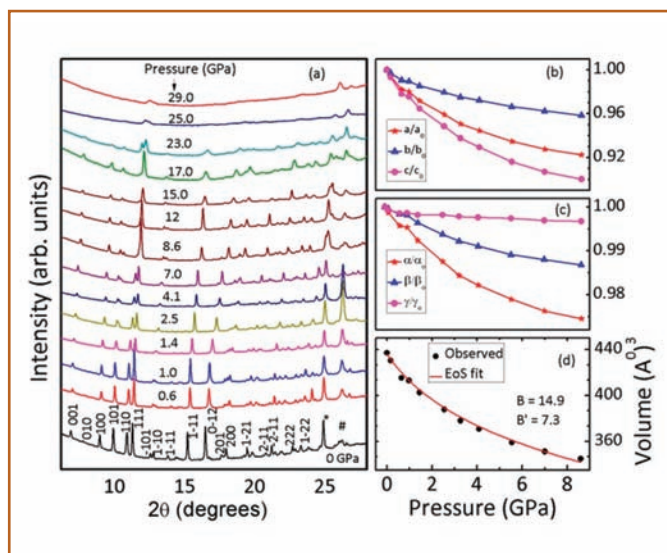


Figure 3. (a) XRD patterns, (b, c) lattice parameters and (d) volume at different pressures

TEX has three conformers viz., exo-exo, exo-endo and endo-endo based on the orientation of the two nitro groups with respect to the six-membered cage (Figure 1). These structures were independently optimized, and we obtained only one minimum corresponding to the structure shown in Figure 1(a). This exo-exo structure yields all positive vibrational frequencies. It is similar to the structure reported using single crystal X-ray analysis, and is termed the  $\alpha$ -phase. Exo-endo (Figure 1(b)) and endo-endo (Figure 1(c)) structures of TEX converged to exo-exo structure during structure optimization. Lattice parameters obtained after structure optimization by CASTEP are comparable with literature reports.

At ambient conditions TEX crystallizes in a triclinic structure (space group  $P\bar{1}$ ) with two formula units per unit cell. Factor group analysis resulted in the following irreducible representations:  $\Gamma_{\text{total}}(144) = 72A_g + 72A_u$ , where  $A_g$  modes are Raman active. Raman spectra of TEX at ambient conditions showed 60 out of the 72 Raman bands that are expected.

From potential energy distribution (PED) obtained using VEDA program, the various bands are assigned. Lattice modes such as 44 and 86  $\text{cm}^{-1}$  that are obtained with only CASTEP are assigned by visualization of the modes using the vibrational analyzer in Materials Studio package. All modes were visualized to validate PED assignments. The observed spectral features of TEX are reasonably well reproduced in the simulated spectrum, notably the strong experimental feature at 301  $\text{cm}^{-1}$  that is assigned to N-N out-of-plane bending mode and the value of the corresponding computed feature is obtained as 286.2  $\text{cm}^{-1}$ .

Several distinct changes in the spectra are observed above 2 GPa: 86, 114, 124 and 142  $\text{cm}^{-1}$  bands (translations) show significant reduction in pressure dependence after 2 GPa (Figure 2); also the doorway modes at (i) 301  $\text{cm}^{-1}$  that is due to out of plane bending of N-N and torsion of NCCN, (ii) 387  $\text{cm}^{-1}$  (in plane bending of NNO) and (iii) 406  $\text{cm}^{-1}$  (in plane bending of NNO and out of plane bending of NCOC) split into doublets at 2.5 GPa. It was noted earlier that only the exo-exo conformation of TEX molecule is stable in Gaussian calculations. It is known that the energy difference between the various phases (such as  $\beta$  and  $\epsilon$ ) of CL-20 at ambient conditions is of the order of a few kcal/mol. The splitting of the 301  $\text{cm}^{-1}$  band in particular indicates the co-existence of exo-exo and exo-endo conformations of the TEX molecule. This exo-exo + exo-endo phase is termed the  $\alpha'$  phase of TEX since there is no change in the crystal structure, as determined from our high pressure XRD studies. This kind of conformational change has been predicted in TEX by DFT calculations at a much higher pressure of 61 GPa. Such discrepancies between experiments and DFT calculations are not uncommon. The nature of 1573  $\text{cm}^{-1}$  N-O asymmetric stretch band changes from soft to hard after 3.5 GPa which is again due to conformational changes in the molecular structure. Around 11 GPa onwards significant changes appear in the Raman spectra. Many medium intensity bands appear at 561, 826, 1024, 1145  $\text{cm}^{-1}$  and weak bands at 372, 999, and 1118  $\text{cm}^{-1}$ . A new band at 561  $\text{cm}^{-1}$  appears near 553  $\text{cm}^{-1}$  (in plane bending of NNO) and it intensifies with pressure. Cage deformation and change in  $\text{NO}_2$  orientation leads to appearance of a new band at 826  $\text{cm}^{-1}$  at 11 GPa. The appearance of new bands at 999, 1024 and 1145  $\text{cm}^{-1}$  could be due to cage deformation. The broad and weak bands

at 2840 and 2940  $\text{cm}^{-1}$  disappear at 11 GPa. The appearance of significantly more number of Raman bands indicates a lowering of the crystal symmetry with more number of molecular units in the primitive cell. The only structure with a lower symmetry than the triclinic  $P\bar{1}$  structure is triclinic with the other space group  $P1$ . The discontinuity in the pressure coefficients of the bands also indicates a possible phase transformation at 11 GPa. The phase above 11 GPa is termed the  $\beta$  phase of TEX. We performed in-situ high pressure XRD measurements on powder samples of TEX up to 29 GPa to confirm the phase transformations indicated by Raman spectroscopy.

The lattice parameters of the triclinic unit cell obtained from the ambient pressure data are in good agreement with those reported in the literature. As the pressure is increased, there are changes in the relative intensities of diffraction peaks that indicate changes in fractional coordinates (Figure 3). Above 10 GPa there are changes in the pattern like merging of doublets into a single peak (at  $2\theta=12^\circ$ ) and triplet to doublet ( $\sim 19.3^\circ$ ). XRD patterns at different pressures were analyzed using GSAS-II software. We could fit the data to the ambient triclinic ( $P\bar{1}$ ) structure up to 8 GPa, indicating that there is no structural phase transition till this pressure. It was not possible to fit to any crystal structure above 8.6 GPa. This pressure corroborates with our Raman spectroscopic results that indicated significant changes in the spectra above 11 GPa. The lattice exhibits highly anisotropic compressive behaviour (Figure 3). The pressure dependence of the lattice parameters shows a change in the slope around 1 GPa. This has correspondence with changes in the Raman spectra around 2 GPa, and can be taken as a precursor to the conformational change from  $\alpha$  to  $\alpha'$  structure. Taking cue from our Raman spectroscopic results, the lattice parameters in the  $\beta$  phase at 15 GPa were obtained with  $P1$  space group by Le Bail fitting with initial values extrapolated from 8.6 GPa using the fitted 3rd order Birch-Murnaghan equation of state (EoS). The changes in the Raman spectra and XRD patterns around 1 GPa are reminiscent of the reversible  $\gamma \rightarrow \zeta$  phase transformation in CL-20 by infrared absorption. This transformation has been reckoned as a conformational, with distinct orientation symmetry of the six nitro-groups with respect to the molecular cage. The  $\alpha$  to  $\alpha'$  transformation seen by us is similar to this. These are new phases of TEX first reported by us.

To determine the thermal expansion coefficient of TEX, its XRD patterns in the temperature range 25 to 150  $^\circ\text{C}$  were recorded using a PANalytical X'Pert Pro MPD X-ray diffractometer with  $\text{Cu K}\alpha$  radiation and secondary beam curved graphite crystal monochromator in the Bragg-Brentano geometry. This was

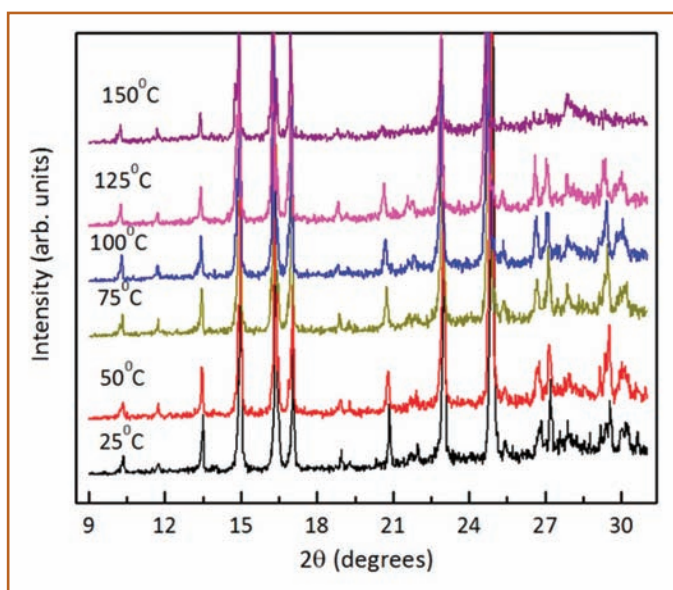


Figure 4. XRD patterns of TEX at different temperatures

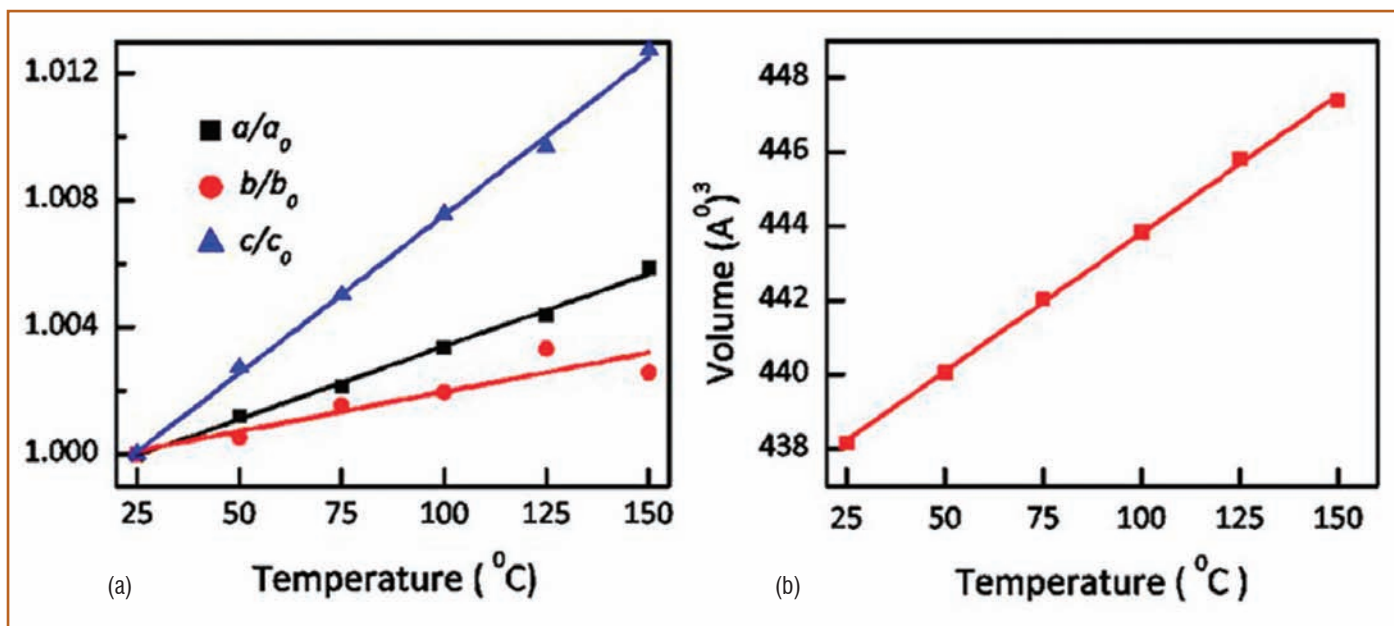


Figure 5. (a) Lattice parameters increase anisotropically with temperature; (b) Volume increases linearly with temperature; straight line represents linear fit to the data points.

coupled with an Anton Paar HTK16 high temperature attachment. About 15 mg of TEX powder was mounted on a tantalum strip that was resistively heated and the sample temperature was monitored with a thermocouple spot welded to the rear of the strip. All measurements were carried out under a vacuum of  $\sim 10^{-5}$  Torr. XRD patterns of TEX during the heating cycle from 25 to 150 °C were recorded in steps of 25 °C. The patterns show normal shift of Bragg peaks to lower  $2\theta$  angles as the temperature is increased, indicating an increase in inter-planar spacing due to thermal expansion (Figure 4).

The crystal structure is fitted to triclinic with space group  $p\bar{1}$  at all temperatures. We have carried out Le-Bail fitting of XRD patterns to obtain the lattice parameters ( $a = 6.850$  Å,  $b = 7.665$  Å,  $c = 8.826$  Å,  $\alpha = 82.38^\circ$ ,  $\beta = 75.0^\circ$ , and  $\gamma = 79.30^\circ$  at 25 °C) as a function of temperature. The lattice parameters obtained at 25 °C with PANalytical X'Pert Pro MPD and STOE X-ray diffractometer are in reasonable agreement with each other. Over the temperature range 25-150 °C, lattice parameter "a" increases by 0.6%, "b" by 0.3%, "c" by 1.3% and the volume by 2.1%. They increase anisotropically with temperature, i.e., the expansion is different in different directions ( $\alpha_a = 4.4 \times 10^{-5}$ ,  $\alpha_b = 3.2 \times 10^{-5}$  and  $\alpha_c = 9.7 \times 10^{-5}$  K<sup>-1</sup>) (Figure 5).

Coefficient of linear thermal expansion and its anisotropy depend on the chemical structure of the molecule, packing structure in the crystal lattice and the chain configuration. Thermal expansion of TEX along the c direction  $\alpha_c$  is 2.2 times  $\alpha_a$  and 3 times  $\alpha_b$ . In the

crystal lattice TEX molecules are linked by C-H...O hydrogen bonds nearly along a and b directions. Van der Waals interaction along the c direction (nearly perpendicular to hydrogen bonds) makes the crystal softer in this direction. The directions of strong and weak hydrogen bonds in the crystal structure can be correlated to thermal expansion anisotropy. Dispersion in hydrogen bond length has been reported for TEX crystal (variation being in the range 2.49 - 2.559 Å), and this difference can be related to the difference in  $\alpha_a$  and  $\alpha_b$ . Volume thermal expansion coefficient  $\alpha_v$  was calculated using a linear least squares fit of V vs. T, where V is the volume of a unit cell of TEX at 25 °C.  $\alpha_v = (1/V)(dV/dT)P = 17.4 \times 10^{-5}$  K<sup>-1</sup>. This is in good agreement with the  $\alpha_v = 11.3 \times 10^{-5}$  K<sup>-1</sup> obtained from the reported volumes of TEX at -173 °C (428.8 Å<sup>3</sup>) and -73 °C (433.64 Å<sup>3</sup>). The latter value of  $11.3 \times 10^{-5}$  K<sup>-1</sup> is slightly lower compared to the one obtained by us since  $\alpha_v$  is expected to reduce at low temperatures following the behaviour of specific heat.

To summarize, we have reported two new high pressure phases of the secondary explosive TEX, viz.,  $\alpha'$  and  $\beta$ , using Raman spectroscopy, X-ray diffraction and first principles calculations. We have also measured the volume thermal expansion coefficient of TEX for the first time, using temperature dependent X-ray diffraction measurements, and find the value to be reasonable, and close to that of a related explosive, CL-20.

Reported by

T. R. Ravindran, Material Science Group

## Young Officer's FORUM

# Study on the Kinetics of the Catalytic Generation of Uranous for Spent Fuel Reprocessing



Shri S. Ramakrishna Reddy joined the Reprocessing Group, Indira Gandhi Centre for Atomic Research in the year 2011 after completing OCES from 5<sup>th</sup> batch of BARC training school, IGCAR campus. He obtained his M.Sc. from Sri Krishna Devaraya University, Andhrapradesh. His main areas of interest are development of materials and methods to be employed for the process improvement, studying the separations of fission products and their extraction kinetics during the reprocessing of spent nuclear fuel. He is currently pursuing Ph.D. with HBNI.

The aqueous reprocessing of spent nuclear fuel by PUREX (Plutonium uranium redox extraction) process involves selective extraction of U(VI) and Pu(IV) by 30% tri-n-butyl phosphate (TBP) in paraffin hydrocarbon as solvent by leaving all other fission products in aqueous nitric acid medium. Further, the mutual separation of U(VI) and Pu(IV) is carried out by reducing Pu(IV) to Pu(III) using uranous(U(IV)) nitrate as a reducing agent. U(IV) is particularly advantageous in that the reaction is fast and it avoids addition of salts that would lead to generation of solid waste. For the preparation of uranous nitrate, electrochemical method is generally being used in most of the reprocessing plants. But this method is kinetically hindered and is inefficient. Further it needs frequent maintenance of the electrodes and is a difficult process

to be scaled up. Hence, there is a need to develop an alternative method for U(IV) generation that would be devoid of the limitations of the electrochemical method.

In our laboratory we are working on development of catalytic methods for uranous preparation. The advantages of the catalytic methods are its fast kinetics, better efficiency, ease of operation and scalability.

In the present work, the kinetics of catalytic reduction of uranyl nitrate to uranous nitrate using hydrazine as a reducing agent in nitric acid medium on Pt/SiO<sub>2</sub> material has been described. Experiments were carried out in a stainless-steel autoclave (Figure 1) as a function of intensity of mixing, temperature, catalyst loading



Figure 1: Experimental set up: SS- autoclave

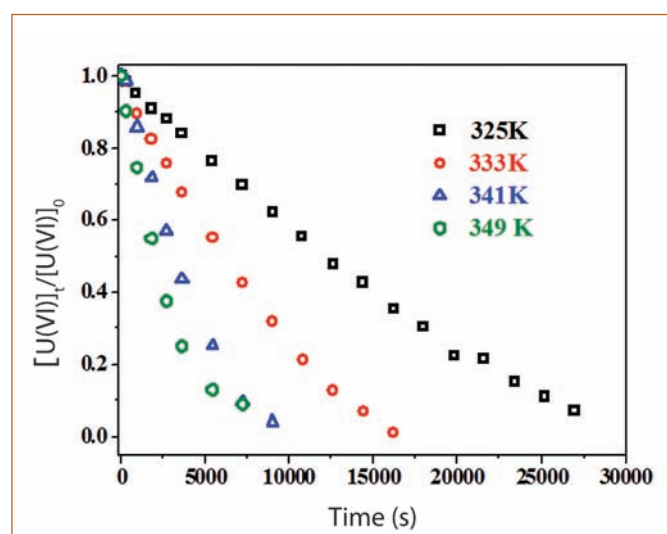


Figure 2: Effect of temperature on the reduction of uranyl ion with hydrazine

and concentrations of nitric acid, hydrazine & uranium. Several kinetic models were derived based on the Langmuir–Hinshelwood approach and each of these was evaluated.

### The effect of impeller speed

Experiments were conducted by varying the speed of agitation (200 to 750 rpm), to quantify the influence of external resistance on the mass transfer. It is found that there is a sharp rise in the rate of the reaction initially up to 500 rpm. Subsequent rise is rather sluggish that the rate of reduction is nearly independent of the impeller speed above 750 rpm. All further experiments were conducted at 750 rpm to determine intrinsic rate parameters.

### Effect of Temperature

The effect of temperature on catalytic reduction of uranyl nitrate by hydrazine was carried out in the range of 325 to 349 K (Figure 2). It could be seen from Figure 2 that the extent of catalytic reduction of uranyl nitrate increases with the increase in reaction temperature. The magnitude of the experimentally determined activation energy would be a guiding value to predict if the reaction is diffusion-controlled or chemical reaction controlled.

The rate of reduction of U(VI) can be expressed in terms of a power rate law as given below,

$$r_v = -\frac{dC_A}{dt} = k' (C_A)^m (C_B)^n (C_C)^p \quad (1)$$

where,  $r_v$  represents the rate of the reaction,  $C_A$ ,  $C_B$  and  $C_C$  represent the concentrations of U(VI), hydrazine and nitric acid respectively, in solution,  $k'$  represents the apparent rate constant for reduction,  $m$ ,  $n$  and  $p$  represents the order of the reaction with respect to respective reactants. Eqn. (1) in natural logarithmic form could be expressed as

$$\ln(r_v) = \ln(k') + m \ln[C_A] + n \ln[C_B] + p \ln[C_C] \quad (2)$$

At time  $t = 0$ , the effect of temperature on the rate of reduction of uranyl ion can be expressed by the Arrhenius equation as given below

$$\ln(r_{v0}) = -\frac{E'_a}{RT} + \ln(k_0) + m \ln[C_{A0}] + n \ln[C_{B0}] + p \ln[C_{C0}] \quad (3)$$

Where, subscript zero represents initial concentrations of

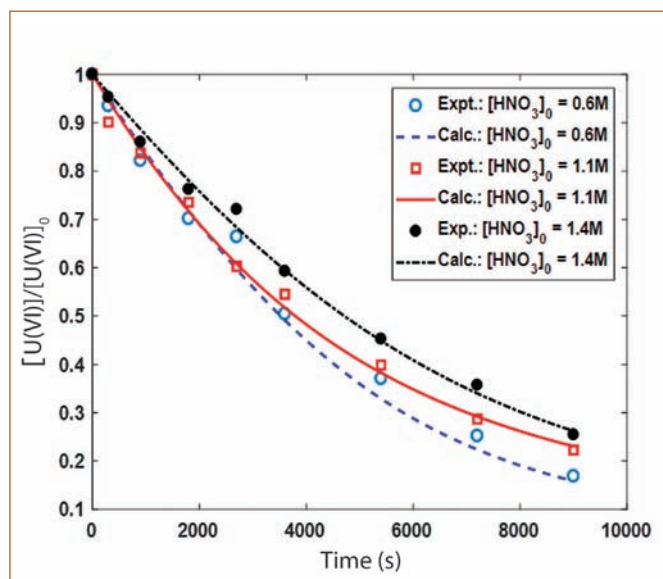


Figure 3: Comparison of experimental and calculated concentration profiles of U

reactants,  $E'_a$  represents the apparent activation energy,  $k_0$  represents pre-exponential factor,  $R$  represents universal gas constant and  $T$  represents the temperature. As the concentrations of reactants were fixed initially, the values of apparent activation energy was estimated from the slope of Arrhenius plot and was found to be about 74.5 kJ/mol. This value of activation energy suggests a possible kinetic controlled regime in the given temperature range. Further, this is in agreement with the values reported in the literature.

### Effect of Catalyst loading

The effect of catalyst loading (40 to 125 kg. m<sup>-3</sup>) on the catalytic reduction of uranyl nitrate was also investigated. It was found that the catalytic reduction of uranyl nitrate in nitric acid medium increases linearly with the catalyst loading. This may be attributed to the increase in the total number of available active sites for the reaction, suggesting that the effect of external mass transfer resistance is rather negligible.

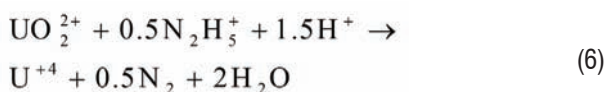
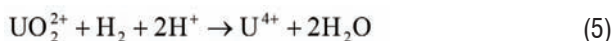
### Effects of Reactants Concentration

The effect of hydrazine (1.1 to 2.4 M), uranium (0.05 to 0.3 M) and nitric acid (0.6 to 2.0 M) concentrations on the catalytic reduction of U(VI) were studied. It is observed that the rate of catalytic reduction of U(VI) increases with increasing concentrations of hydrazine and U(VI) initially and subsequently it flattens. It may be due to the saturation of the catalyst surface. On the other hand initial reduction rate of uranyl nitrate is found to decrease with increase in concentration of nitric acid. This is probably because

of the oxidising attribute of nitric acid, especially when it is present in excess.

### Reaction Stoichiometry

Following reactions (4) to (7) take place during the catalytic reduction of uranyl ion with hydrazine;



In a generic form Eqn. (6) could be written as,



### Kinetic Model of the Reaction

Langmuir-Hinshelwood (L-H) type model was proposed to describe the reduction of U(VI) to U(IV). Several model equations were derived based on the assumption that one of the three elementary steps of the reduction process (adsorption of reactants, surface reaction between adsorbed molecules and desorption of products) would be the rate-controlling step. Kinetic models for those different controlling mechanism are given in Table 1.

### Model Parameter Estimation

The values of the intrinsic rate parameter, adsorption equilibrium constants pertaining to different -model equations were

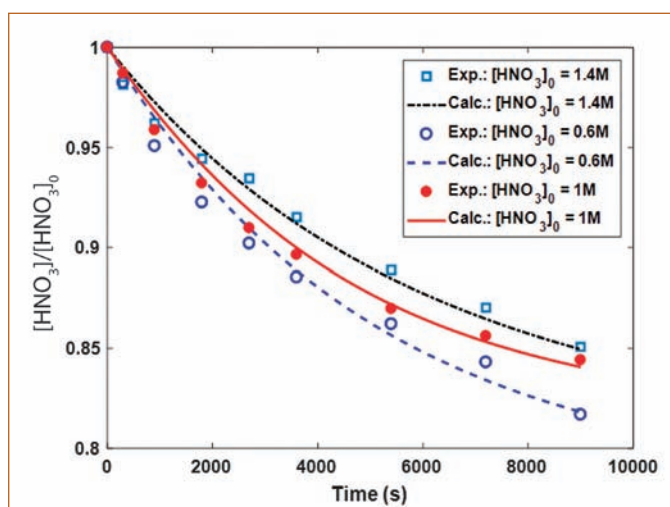


Figure 4. Comparison of experimental and calculated concentration profiles of nitric acid

performed using MATLAB. The model considering the reaction of adsorbed reactants namely Uranium, nitric acid and hydrazine on the catalyst surface and with the surface reaction as the rate controlling step, could be expressed analytically by using Eqn. (8)

$$r_A = \frac{kK_A^2 K_B K_C^3 C_A^2 C_B C_C^3}{(1 + K_A C_A + K_B C_B + K_C C_C)} \quad (8)$$

Where,  $k$  represents rate constant  $K_A, K_B$  and  $K_C$  represents adsorption equilibrium constants and  $C_A, C_B$ , and  $C_C$  represents concentration of U(VI), nitric acid and hydrazine respectively.

Table1. Kinetic models for the different controlling mechanism

Controlling mechanism	Rate equation
All the reactants molecularly adsorbed on the catalyst surface and reacts	
1. Adsorption of A controlling.	$r_A = \frac{kC_A}{(1 + K_B C_B + K_C C_C)}$
2. Adsorption of B controlling.	$r_A = \frac{kC_B}{(1 + K_A C_A + K_C C_C)}$
3. Adsorption of C controlling	$r_A = \frac{kC_C}{(1 + K_A C_A + K_B C_B)}$
4. Surface reaction controlling	$r_A = \frac{kK_A^2 K_B K_C^3 C_A^2 C_B C_C^3}{(1 + K_A C_A + K_B C_B + K_C C_C)^6}$
Uranyl species(A) present in the solution interacts with hydrazine(B) and nitric acid(C) adsorbed on the catalyst surface	
5. Adsorption of B controlling	$r_A = \frac{kC_B}{(1 + K_C C_C)}$
6. Adsorption of C controlling	$r_A = \frac{kC_C}{(1 + K_B C_B)}$
7. Surface reaction controlling	$r_A = \frac{k.K_B.K_C^3.C_A^2.C_B.C_C^3}{(1 + K_B C_B + K_C C_C)^4}$

Figures 3 and 4 show comparisons between experimental and estimated results from the model IV for some of the typical case. Based on these observations, it is appropriate to conclude that the surface reaction between the adsorbed reactants, viz; uranium, hydrazine and nitric acid, on the surface of the catalyst controls the rate of catalytic reduction of U(VI). By this process more than 95% conversion could be achieved in about 3 hours.

Reported by

S. Ramakrishna Reddy, Reprocessing Group

## Young Researcher's Forum



Dr. Aditi Chandrasekar has completed her Ph.D under HBNI-IGCAR in 2019. She worked on the experimental and quantum chemical aspects of nuclear fuel reprocessing in Fuel Chemistry Division, MC&MFCG, IGCAR. She has done her Integrated B.S-M.S from Indian Institute of Science Education and Research - Kolkata (IISER-K). She has eight peer reviewed journal publications.

# Trends in Small Angle Neutron Scattering of Actinide – Trialkyl Phosphate Complexes: A Molecular insight into Third Phase Formation

The Small Angle Neutron Scattering (SANS) technique has been employed for a variety of applications, including study of polymers, organic molecules, gels, micro and nanoscale materials and bio molecules. Subsets of these that pertain to the current work include, probing aggregation behaviour of micelles, cloud point studies and temperature dependent aggregation. Such aggregation leading to third phase formation during extraction of Th(IV) by organophosphates is a concern during the processing of Th(IV) solutions.

Tri-sec-butyl phosphate (TsBP) has shown higher U/Th separation factor and lesser third phase formation tendency compared to its isomers, Tri butyl phosphate (TBP) and tri-iso-butyl phosphate (TiBP). Tri-sec-amyl phosphate (TsAP), on the other hand, does not form third phase with both U(VI) and Th(IV) up to saturated

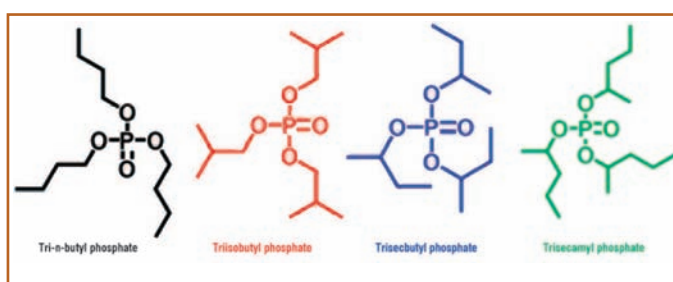


Figure 1: Structure of trialkyl phosphates studied in the present work

metal concentrations when extracted from 1M nitric acid at 303 K. In the present work, SANS studies have been carried out using solutions of TBP, TiBP, TsBP and TsAP in  $n\text{-C}_{12}\text{D}_{26}$  (deuterated dodecane) loaded with U(VI) as well as Th(IV). The structures of the trialkyl phosphates (TalP) used in this study are shown in Figure 1. The variation in the SANS profiles, stickiness parameter and attraction potential energy have been examined as a function of three parameters influencing third phase formation phenomena. The effects of extractant structure, metal ion concentration and temperature have been systematically investigated.

### SANS Measurement

For the SANS measurements, organic phase containing metal complexes of known concentration in 1.1 M TalP/ $n\text{-C}_{12}\text{D}_{26}$  was used. The neutron scattering experiments were carried out using the SANS facility at Dhruva reactor, Bhabha Atomic Research Centre (BARC), India. A mean neutron wavelength of 5.2 Å with a resolution of ~ 15 % was used for the experiments. The scattered neutrons were measured using a one-dimensional  $^3\text{He}$  gas detector. The samples were scanned in the Q range from 0.017 to 0.35 Å<sup>-1</sup>. A quartz cell with a thickness of 2 mm was used for holding the samples during the measurements. The diameter of the micelle ( $\sigma$ ), was calculated mathematically assuming the particles as spherical and the width of the square-well potential ( $\Delta$ ), is taken as 3 Å for the

potential energy calculations. As third phase formation is inherently an aggregation phenomenon, sticky hard sphere model has been used to fit the data for these systems.

The concentrations of U(VI) and Th(IV) in the organic phase were varied so as to approach the third phase region with increasing metal concentration and test the aggregation parameters. The concentration of metal ions (Th and U) and  $\text{HNO}_3$  of samples used for SANS experiments are shown in Table 1.

Table 1: Concentration of metal ions/acid in the samples used for SANS experiments

Organic phase	Concentration of metal ion (g/L)		Metal free samples
	U(VI)	Th(IV)	
1.1M TBP/ $n\text{-C}_{12}\text{D}_{26}$	20	20	0.23
	30	30	
	40	40	
	120	40	
1.1M TiBP/ $n\text{-C}_{12}\text{D}_{26}$	20	20	0.20
	30	30	
	40	40	
	120	40	
1.1M TsBP/ $n\text{-C}_{12}\text{D}_{26}$	20	20	0.26
		40	
1.1M TsAP/ $n\text{-C}_{12}\text{D}_{26}$	40	20	0.22
	80	30	

### Aggregation behaviour of $\text{Th}(\text{NO}_3)_4$ systems

#### Effect of the structure of trialkyl phosphate

The scattering intensity for Th(IV) loaded samples changes with variation in the structure of the extractant, when all other factors are kept constant. Figure 2 shows the scattering profiles obtained at 303K for various TalP/  $n\text{-C}_{12}\text{D}_{26}$  systems, all loaded with same amount of metal ion (30 g Th(IV)/L). The highest scattering intensity in the low Q region is shown by TBP followed by TiBP, TsBP and TsAP respectively. The stickiness parameter  $\tau^{-1}$  and the attractive potential energy  $U_0$  calculated for the four systems are shown (Table 2a). Highest stickiness parameter was observed with TBP, which has higher third phase formation tendency with Th(IV). The interaction potential energy is the most negative indicating higher attraction between the micelles. The stickiness parameter decreases with branching in the alkyl chain as in the case of TiBP and is further lower for TsBP, which has lower third phase formation tendency with Th(IV). For TsAP, the value of stickiness parameter

drops much lower and it is also observed from solvent extraction experiments that TsAP does not form third phase with Th(IV), when extracted from 1M  $\text{HNO}_3$  at all concentrations of metal ion. Based on the experimentally derived metal–ligand ratio in the complex, aggregation number was taken as 3 for Th(IV) complexes. An aggregate diameter of 13.8 Å was obtained for TBP, TiBP and TsBP and a diameter of 14.6 Å for TsAP, based on the assumption that the micelles are spherical as discussed above. For a given system, the size of the aggregate did not change, though the potential varied depending on the conditions. This has been previously reported in the literature which showed that aggregate number changed only in the particle growth model applied to higher metal loading, e.g. third phase regions. Our studies, however, are restricted to lower metal loading where radii remain constant as consistent with earlier study.

#### Effect of metal loading

For a given extractant system, the scattering intensity, stickiness parameter and attraction potential energy change with the change in concentration of the metal ion. At higher concentration of Th(IV) in the organic phase (40 g/L), scattering intensity in the low Q region is highest for all extractant systems at a fixed temperature of 303 K, (Figure 3 (A–D)). The TBP system shows highest scattering intensity for a given metal loading, and least for TsAP system. The difference in intensity between metal loading of 20g/L and 40g/L is most pronounced in the case of TBP (Figure 3(C)), which has the highest tendency to form third phase and the least difference was observed for TsAP system, which does not form third phase with Th(IV)/1M  $\text{HNO}_3$  at all thorium concentrations. From the patterns, it can be seen that for extractants such as TBP and TiBP which

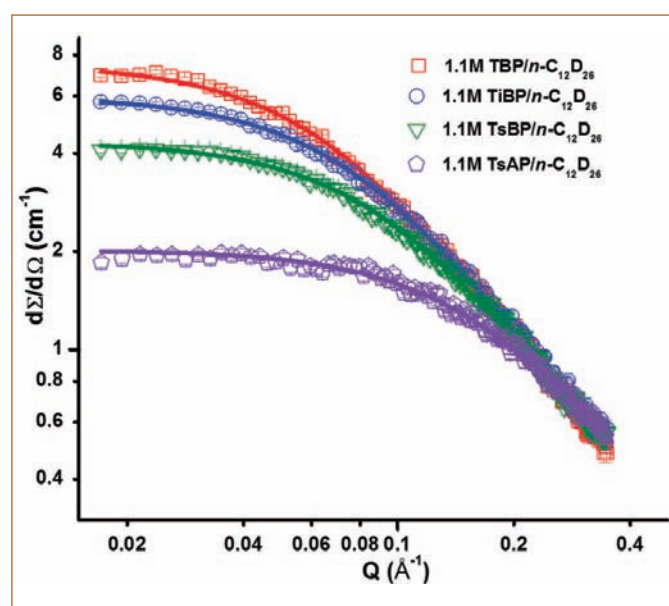


Figure 2: SANS data obtained for the 1.1 M TalP/ $n\text{-C}_{12}\text{D}_{26}$  -  $\text{Th}(\text{NO}_3)_4$ /1M  $\text{HNO}_3$  systems loaded with 30 g Th/L at 303 K.

Table 2: The fitted parameters of SANS data for (a) 1.1 M TalP/n-C<sub>12</sub>D<sub>26</sub> - Th(NO<sub>3</sub>)<sub>4</sub>/1M HNO<sub>3</sub> systems, loaded with 30g/L of Th(IV) at 303 K. (b) 20g/L and 40g/L Th(IV) loaded TalP/ n-C<sub>12</sub>D<sub>26</sub> systems at 303 K. (c) 1.1 M TalP/n-C<sub>12</sub>D<sub>26</sub> - Th(NO<sub>3</sub>)<sub>4</sub>/1M HNO<sub>3</sub> systems, loaded with 40g Th/L as a function of temperature.

a) Conditions: TalP/n-C<sub>12</sub>D<sub>26</sub> /1M HNO<sub>3</sub> systems, loaded with 30 g/L of Th(IV) at 303 K.

System	Aggregation number (N)	Aggregate Diameter (D) (Å)	Stickiness Parameter (1/τ)	Potential Energy [U <sub>0</sub> (kBT)]
1.1 M TBP/n-C <sub>12</sub> D <sub>26</sub>	3	13.8	9.3	-1.47
1.1 M TiBP/n-C <sub>12</sub> D <sub>26</sub>	3	13.8	8.5	-1.38
1.1 M TsBP/n-C <sub>12</sub> D <sub>26</sub>	3	13.8	7.7	-1.28
1.1 M TsAP/n-C <sub>12</sub> D <sub>26</sub>	3	14.6	4.7	-0.84

b) Conditions: 20g/L and 40g/L Th(IV) loaded TalP/ n-C<sub>12</sub>D<sub>26</sub> systems at 303 K.

Metal Conc.	TBP (N = 3, D = 13.8 Å)		TiBP (N = 3, D = 13.8 Å)		TsBP (N = 3, D = 13.8 Å)		TsAP (N = 3, D = 14.6 Å)	
	1/τ	U <sub>0</sub> (k <sub>B</sub> T)	1/τ	U <sub>0</sub> (k <sub>B</sub> T)	1/τ	U <sub>0</sub> (k <sub>B</sub> T)	1/τ	U <sub>0</sub> (k <sub>B</sub> T)
20g/L	7.4	-1.24	7.3	-1.23	6.9	-1.17	4.6	-0.81
40g/L	11.3	-1.66	9.2	-1.46	8.9	-1.42	4.9	-0.87

c) Conditions: 1.1 M TalP/n-C<sub>12</sub>D<sub>26</sub> - Th(NO<sub>3</sub>)<sub>4</sub>/1M HNO<sub>3</sub> systems, loaded with 40 g Th/L

Temp(K)	TBP (N = 3, D = 13.8 Å)		TiBP (N = 3, D = 13.8 Å)		TsBP (N = 3, D = 13.8 Å)	
	1/τ	U <sub>0</sub> (k <sub>B</sub> T)	1/τ	U <sub>0</sub> (k <sub>B</sub> T)	1/τ	U <sub>0</sub> (k <sub>B</sub> T)
313	9.8	-1.52	8.4	-1.37	8.0	-1.32
323	8.8	-1.41	7.6	-1.27	7.5	-1.25
333	7.8	-1.29	7.2	-1.21	6.9	-1.17

have higher third phase formation tendency, the scattering intensity is more sensitive to variation with metal ion concentration in the organic phase.

When the metal loading is higher, the tendency for the system to form third phase is higher, because of the stronger attractive interaction between the metal solvate species while approaching the LOC. When the number density of particles increase, they are forced to pack in such a way that they come closer, making this a factor for aggregation. In general, the attraction leading to third phase formation / aggregation can be prevented in metal-extractant systems by increasing the alkyl chain length of the extractant molecules, thus enhancing the intermicellar distance making the central polar cores stay away from each other. In addition, for systems consisting of isomers of extractants with similar micellar radius, the structure of the extractant may influence the intermicellar distance, in a way this is achieved by introducing branching on the carbon chain close to the polar core. Thus the stickiness parameter increases from 7.7 in TsBP to 9.3 in TBP system. It is interesting to note that even in the nanoparticle systems, these are often capped with sterically bulky molecules to prevent them from coming close

together, greatly reducing their tendency to aggregate. For the four extractant systems (Figure 3), stickiness parameters have been computed and the results are shown in Table 2(b). As expected, the stickiness parameter is higher at 40g/L metal loading as compared to 20g/L for all the extractants. The attraction potential is larger at higher metal concentrations (40 g/L), indicating more attraction between the micelles. Among the extractants, TBP has the highest stickiness, followed by TiBP, TsBP and TsAP. This trend matches with the trends observed in solvent extraction experiments, which showed a similar trend for third phase formation tendency among these extractants. Stickiness parameter is markedly lower for TsAP than the other three phosphate systems with butyl carbon chain, indicating that its third phase limits are higher. This has been observed by earlier solvent extraction experiments carried out in our laboratory.

#### Effect of temperature

Apart from investigating the effects of structure of alkyl groups of the extractant and organic metal loading on neutron scattering, effect of temperature was also probed in the present work using the same tool, keeping all other factors similar. Figure 4 (A, B and C) shows

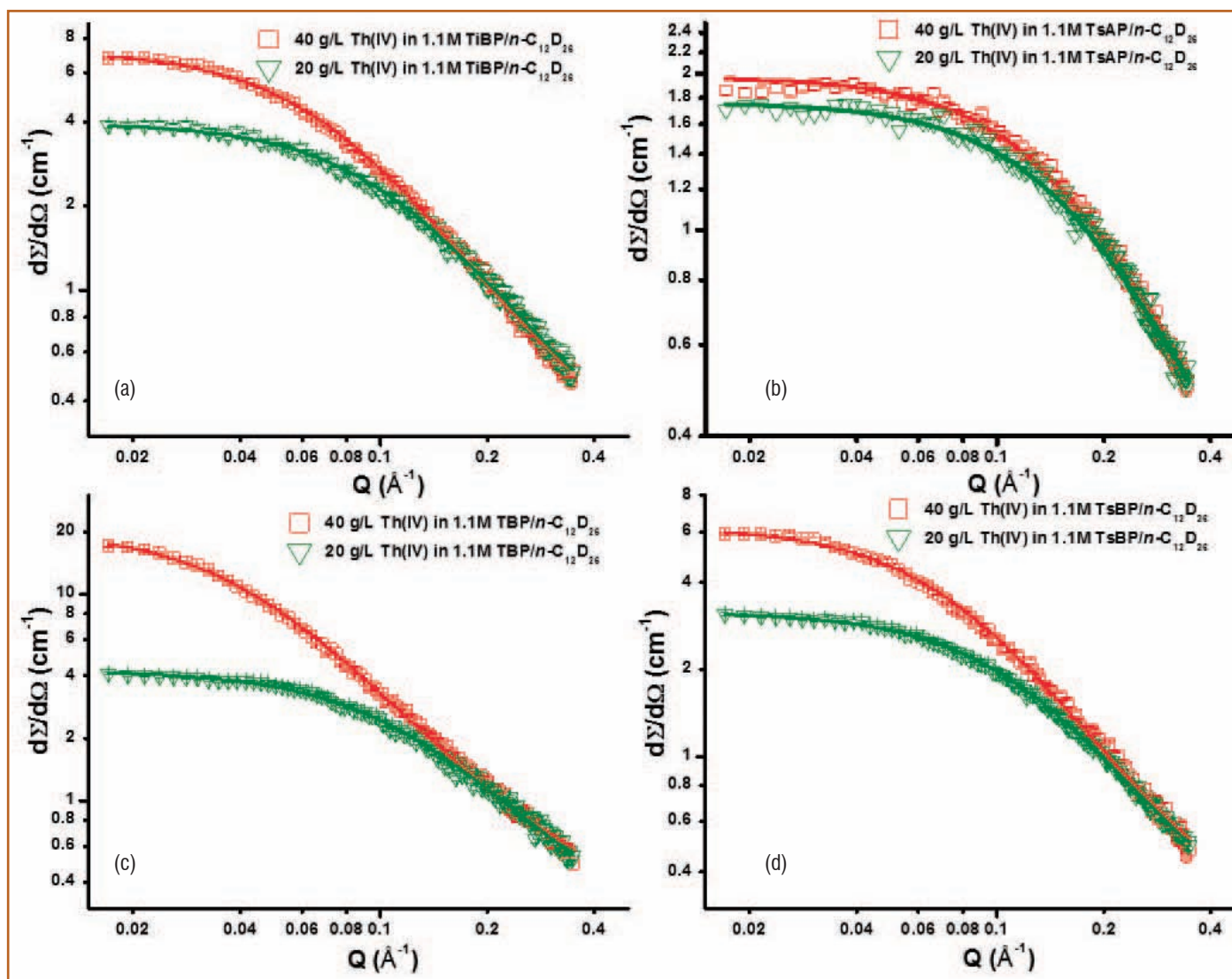


Figure 3: SANS plots of 1.1 M TalP/n-C<sub>12</sub>D<sub>26</sub> - Th(NO<sub>3</sub>)<sub>4</sub>/1M HNO<sub>3</sub> systems with organic Th(IV) loading of 20g/L and 40g/L at 303 K . (a) TiBP (b) TsAP (c) TBP and (d) TsBP

the variation in SANS patterns for TBP, TiBP and TsBP systems, as the temperature was increased from 313 to 343 K in steps of 10 degrees. For all the extractant systems, the Th(IV) concentration was kept at 40 g/L. As the temperature was increased, the intensity of scattering monotonically reduced for all the extractants. Among these, TBP system is most sensitive to increase in temperature from 313 to 323 K, as well as from 323 to 333 K.

The increase in thermal energy suppresses aggregation in the solvent phase and hence prevents third phase formation. Thus, aggregation leading to third phase formation can be minimised by increasing the temperature as observed by our earlier solvent extraction experiments. The variations in stickiness parameter and attraction potential energy as a result of temperature increase are shown in Table 2(c). The data indicate that there is a gradual decrease in the stickiness parameter with increase in temperature for all the three solvents.

## Investigations on UO<sub>2</sub>(NO<sub>3</sub>)<sub>2</sub> systems

### Effect of metal loading

The third phase formation tendency of Th(IV) complexes showed a strong correlation with the stickiness parameter obtained from the SANS patterns. It has been observed from solvent extraction experiments that U(VI) does not form third phase with the 1.1M TalP/n-C<sub>12</sub>D<sub>26</sub> in the extraction from 1M HNO<sub>3</sub>. Hence to investigate our predictions, similar SANS experiments were carried out using samples loaded with U(VI). Figure 5 shows the fitted SANS plots obtained at 303 K from TiBP, TBP and TsAP systems, respectively, as a function of increasing U(VI) concentration in the organic phase. TiBP and TBP systems were loaded with 20, 30 and 40g/L of U(VI). From the profiles it can be seen that there is a marginal increase in the scattering intensity as metal concentration was increased for all the three extractants. Stickiness parameter and attraction potential

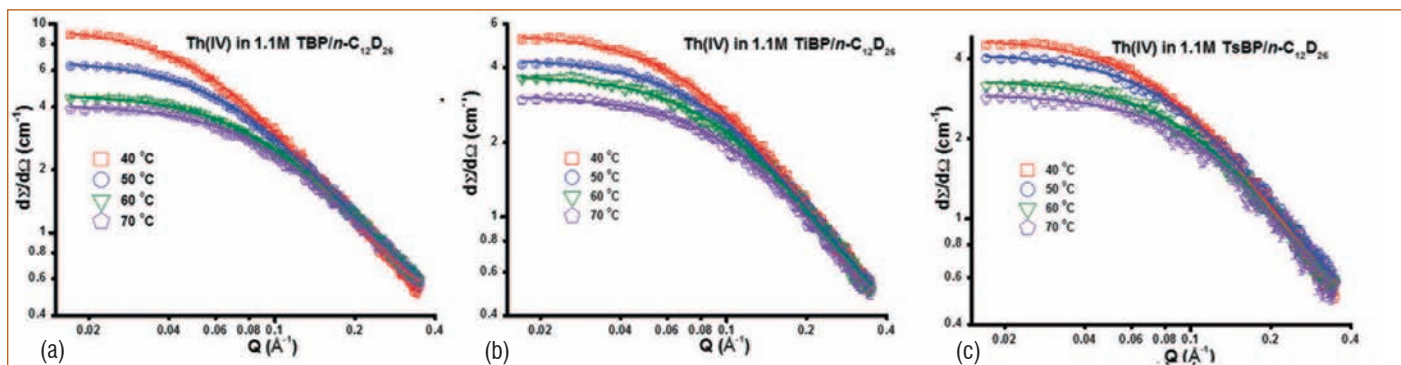


Figure 4: Variation in the scattering pattern as a function of temperature for 1.1 M TaBP/n-C<sub>12</sub>D<sub>26</sub>-Th(NO<sub>3</sub>)<sub>4</sub>/1M HNO<sub>3</sub> systems with a Th(IV) loading of 40 g/L in the organic phase. (a) TBP (b) TiBP (c) TsBP systems.

energy have been calculated for all metal concentrations (Figure 4(A to C)) (Table 3(A)). For all the extractant systems, there is a small change in the stickiness and aggregation energy as the metal loading is increased, indicating that aggregation tendency of U(VI) loaded organic phase have a limited sensitivity to increasing metal loading. Aggregation number was taken as 2 for all extractant systems loaded with U(VI). For TBP and TiBP, the micelle diameter obtained was 12.0 Å, and for TsAP it was calculated to be 12.7 Å.

As 10g/L change in U(VI) had only a small effect on the intensity and fitted parameters obtained from the curves, 1.1M TsAP/n-C<sub>12</sub>D<sub>26</sub> was loaded with 40 and 80g/L of U(VI). Figure 5(C) shows the SANS results obtained from these two systems and Table 3(A) shows the corresponding  $\tau^{-1}$  and  $U_0$  values. The magnitude of  $\tau^{-1}$  is lower for TsAP compared to TBP and TiBP, illustrating that its tendency to form third phase is even lower than the two butyl phosphates. It has also been observed experimentally that phosphates with a longer carbon chain are less susceptible to third phase formation.

At lower concentrations of U(VI) in the organic phase, the stickiness parameter was lower, because at the given acid concentration, these extractants do not form third phase with uranium even with saturated aqueous concentration of the metal ion. SANS studies

were carried out with samples loaded with 120 g/L of U(VI), which was the organic loading obtained with near saturated (saturated loading ~ 120 – 125 g/L) aqueous concentration of the metal ion. The data in Table 3(B) show the calculated values of  $\tau^{-1}$  and  $U_0$  obtained at 303 K from TBP, TiBP and TsAP systems loaded with 120 g/L of U(VI) after fitting the data.

**Effect of temperature on U(VI) system**

Increase in temperature lowers the stickiness in the Th(IV) systems, thereby reducing the third phase formation tendency. The effect of raising the temperature has a similar effect on U(VI) loaded organic phases containing 1.1M TaBP/n-C<sub>12</sub>D<sub>26</sub>. For all the extractants, for a fixed metal loading, the scattering intensity decreases with increase in temperature. Table 3c shows that for all three phosphates, the stickiness parameter decreases with increase in temperature as enhancement in thermal energy reduces inter-particle attraction. The attractive energy becomes less with temperature rise.

**Comparing U(VI) and Th(IV) SANS**

As described in the previous sections, TBP and TiBP have high tendency to form third phase with Th(IV), whereas they do not form third phase with U(VI) under normal extraction conditions. The SANS patterns obtained in the present study are in line with the above

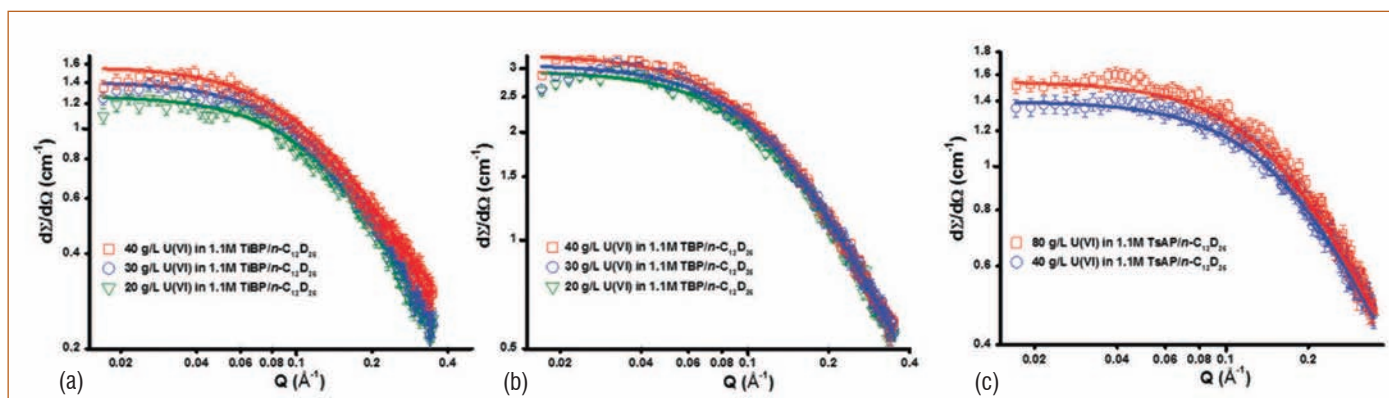


Figure 5: Variation of SANS curves as a function of metal loading obtained from 1.1 M TaBP/n-C<sub>12</sub>D<sub>26</sub>-UO<sub>2</sub>(NO<sub>3</sub>)<sub>2</sub>/1M HNO<sub>3</sub> systems at 303 K (a) TiBP (b) TBP and (c) TsAP.

Table 3: The fitted parameters of SANS data for (a) 1.1 M TalP/n-C<sub>12</sub>D<sub>26</sub>-UO<sub>2</sub>(NO<sub>3</sub>)<sub>2</sub>/1M HNO<sub>3</sub> systems at 303 K. (b) 1.1 M TalP/n-C<sub>12</sub>D<sub>26</sub>-UO<sub>2</sub>(NO<sub>3</sub>)<sub>2</sub>/1M HNO<sub>3</sub> systems loaded with 120 g U/L at 303 K. (c) 1.1 M TalP/n-C<sub>12</sub>D<sub>26</sub>/1M HNO<sub>3</sub> systems with U(VI): 40 g/L in TBP and TiBP and 20 g/L in TsBP as a function of temperature. (d) 1.1 M TBP and TiBP in C<sub>12</sub>D<sub>26</sub> loaded with 40 g/L Th(IV) and U(VI)/1M HNO<sub>3</sub> at 308 K.

a) Conditions: 1.1 M TalP/n-C <sub>12</sub> D <sub>26</sub> – UO <sub>2</sub> (NO <sub>3</sub> ) <sub>2</sub> /1M HNO <sub>3</sub> at 303 K						
U(VI) conc. (g/L)	TBP(N = 2, D = 12.0 Å)		TiBP(N = 2, D = 12.0 Å)		TsAP(N = 2, D = 12.7 Å)	
	1/τ	U <sub>0</sub> (k <sub>B</sub> T)	1/τ	U <sub>0</sub> (k <sub>B</sub> T)	1/τ	U <sub>0</sub> (k <sub>B</sub> T)
20	6.6	-1.02	6.6	-1.01	–	–
30	6.7	-1.03	6.8	-1.04	–	–
40	6.9	-1.06	7.2	-1.10	4.7	-0.72
80	–	–	–	–	4.9	-0.76

b) Conditions: 1.1M TalP/n-C <sub>12</sub> D <sub>26</sub> /1M HNO <sub>3</sub> systems loaded with 120 g U/L at 303 K				
System	Aggregation number (N)	Aggregate Diameter (D)	Stickiness Parameter (1/τ)	Potential Energy [U <sub>0</sub> (k <sub>B</sub> T)]
1.1 M TBP/n-C <sub>12</sub> D <sub>26</sub>	2	12.0	7.9	-1.2
1.1 M TiBP/n-C <sub>12</sub> D <sub>26</sub>	2	12.0	7.9	-1.2
1.1 M TsAP/n-C <sub>12</sub> D <sub>26</sub>	2	12.7	5.2	-0.81

c) Conditions: 1.1 M TalP/n-C <sub>12</sub> D <sub>26</sub> /1M HNO <sub>3</sub> systems with U(VI): 40g/L in TBP and TiBP and 20g/L in TsBP						
Temp(oC)	TBP		TiBP		TsBP	
	1/τ	U <sub>0</sub> (k <sub>B</sub> T)	1/τ	U <sub>0</sub> (k <sub>B</sub> T)	1/τ	U <sub>0</sub> (k <sub>B</sub> T)
40	5.5	-0.84	5.4	-0.82	5.3	-0.79
50	5.1	-0.76	4.9	-0.71	4.8	-0.69
60	5.0	-0.74	4.8	-0.70	-	-

d) Conditions: 1.1 M TBP and TiBP in C <sub>12</sub> D <sub>26</sub> loaded with 40g/L Th(IV) and U(VI)/1M HNO <sub>3</sub> at 308 K					
Metal ion in the organic phase TBP		1.1 M TBP/n-C <sub>12</sub> D <sub>26</sub>		1.1 M TiBP/n-C <sub>12</sub> D <sub>26</sub>	
		1/τ	U <sub>0</sub> (k <sub>B</sub> T)	1/τ	U <sub>0</sub> (k <sub>B</sub> T)
40g/L Th(IV)		10.9	-1.63	8.7	-1.40
40g/L U(VI)		5.8	-0.89	5.5	-0.83

behaviour and show a clear difference between organic phases loaded with Th(IV) and U(VI) for these two extractant systems. Figure 6 (A and B) shows the SANS plot obtained at 308 K for TBP and TiBP systems, respectively. Each organic phase was separately loaded with 40g/L of Th(IV) and U(VI). It can be seen that for both the extractant systems, the scattering intensity is much higher for Th(IV) loaded samples as compared to samples loaded with U(VI). The data in Table 3d shows the corresponding stickiness parameter and attraction potential energy obtained for the above systems. The stickiness parameter was found to be much higher for the Th(IV) loaded samples indicating a higher third phase formation tendency, whereas for the U(VI) loaded samples, stickiness is much lower, in agreement with the observation that two extractant systems do not form third phase with U(VI). From the SANS studies it is observed that tetravalent metals ions with higher ionic potential e.g. Th(IV) have higher tendency to form third phase.

### Predictions on third phase formation

#### Interpretation of scattering intensity and stickiness parameter

Observations made from the SANS studies can be extended to predicting the likelihood of third phase formation phenomena. TBP loaded with upto 120g/L of U(VI) showed scattering intensity ( $Q \rightarrow 0$ ) less than 3.5, indicating that in general for systems with scattering intensity below 3.5 they are far from forming third phase. On the other extreme, systems with scattering intensity ( $Q \rightarrow 0$ ) above 6 are close to the third phase limit as seen from Figure 3(A), which shows the scattering for TiBP loaded with 40g/L of Th(IV), which is close to its limiting organic concentration of 43.8g/L. Similar threshold values can be set for the stickiness parameter  $\tau^{-1}$ . Systems with  $\tau^{-1}$  less than 8 are not susceptible to third phase formation as seen from Table 3(b), whereas a stickiness value greater than 9 would signal near third phase conditions. This can

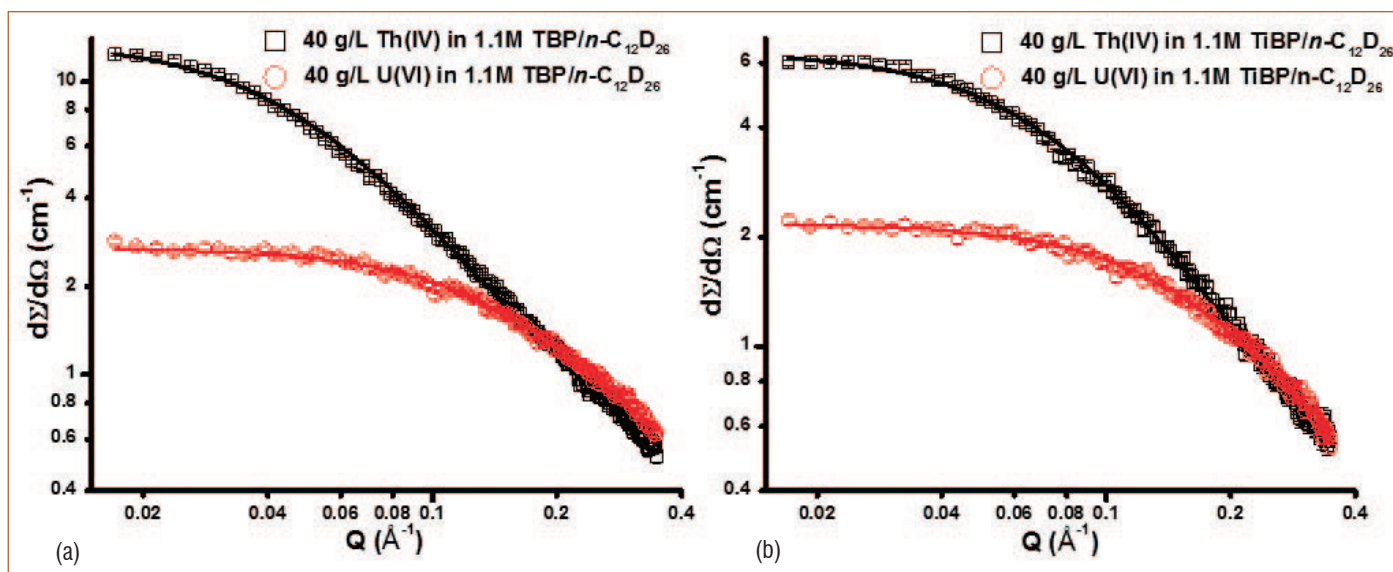


Figure 6: SANS patterns obtained at 308 K from 1.1 M TaIP/C<sub>12</sub>D<sub>26</sub> (a) TBP and (b) TiBP loaded with 40g/L Th(IV) and U(VI)/1M HNO<sub>3</sub>.

be seen from Table 2(b) which shows 9.2 to be the stickiness parameter for TiBP system loaded with 40g/L of Th (IV). Stickiness parameter for TBP is much higher than the threshold when loaded with 40g/L of Th(IV) which is close to its limiting organic concentration. The corresponding value for TsAP loaded with 40g/L Th(IV) is 4.9 which is much below the threshold, and agrees with the observations that TsAP does not form third phase with Th(IV) at 1M acid up to saturated aqueous concentration.

#### Effect of the extracted metal ion

Tetravalent metal ions e.g. Th(IV) have higher tendency to form third phase as seen from its higher scattering intensities and stickiness parameter data. In this context, for the Zr(IV)–TBP system as it has been experimentally shown in our laboratory that Zr is bound to form third phase even at much lower metal ion concentration for e.g. above the LOC of 8.19g/L. The studies on SANS of 1.1M TBP/n-C<sub>12</sub>D<sub>26</sub> loaded with Zr (0.057 mol/L) before the LOC conditions indicated a scattering intensity of around 5 ( $Q \rightarrow 0$ ) with a stickiness parameter of 9.7 and potential energy of  $-1.4$ . The above values of Zr-TBP system are higher than the corresponding values (stickiness parameter = 7.4 and potential energy =  $-1.24$ ) reported in the present study for TBP-Th(IV) system loaded with higher Th concentration (20 mg Th/L which corresponds to 0.086 mol/L) with a scattering intensity of around 4 ( $Q \rightarrow 0$ ).

#### Temperature and third phase formation

Increasing temperature decreases the scattering intensity as well as stickiness parameter. From these studies it is observed that TiBP system loaded with 40g/L of Th (IV), at 313K its stickiness parameter is below the third phase limit of 9, and beyond 323K,

$\tau^{-1}$  falls below 8. It could be possible that systems with stickiness parameter below 8 are not susceptible to third phase formation. Temperatures above 343K were not investigated in the present work as it is generally not recommendable operating temperature for solvent extraction system due to safety issues when employed under plant conditions.

#### Predictions when diluent is changed

Extending the diluent chain length decreases the LOC value for Th(IV). Hence, experiments with longer chain length diluents, e.g. tetradecane instead of dodecane, can lead to higher scattering intensity and  $\tau^{-1}$  for the given metal loading especially with Th(IV) system. Similarly, diluents with shorter chain length such as octane or decane, is expected to reduce scattering intensity at low region and stickiness.

SANS experiments were carried out to investigate the third phase formation tendency for 1.1M TaIP extractants in deuterated dodecane. Three factors affecting third phase formation were investigated in this study: nature of extractant, nature of metal ion and temperature. Comparison between U(VI) and Th(IV) complexes with the same extractant and comparison between the different phosphate extractants loaded with a given metal ion have been studied for the first time. The results obtained are in good agreement with our earlier solvent extraction experiments with respect to all the three parameters that were investigated. Further, the intensity of scattering and stickiness parameter data can be used for predicting the tendency of a system to form third phase. This study was also extended to set threshold values for scattering intensity and stickiness parameter below which third phase will not form, as well as the thresholds above which third phase is expected to form.

## Conference and Meeting Highlights

**International Conference on  
Nanostructuring by Ion Beams (ICNIB-2019)  
IGCAR, Kalpakkam  
November 6-8, 2019**



Release of the Book of Abstracts (L to R) Dr. G. Amarendra, Chairman, ICNIB-2019, Prof. Avinash Chandra Pandey, Director, Inter-University Accelerator Centre, New Delhi, Dr. B. K. Panigrahi, Co-Chairman and Dr. C. David, Convener

The 5<sup>th</sup> International Conference on Nanostructuring by Ion Beams (ICNIB-2019) was organized by Indira Gandhi Centre for Atomic Research (IGCAR) in association with Board of Research in Nuclear Sciences (BRNS), Ion Beam Society of India (IBSI), Inter-University Accelerator Centre (IUAC) and Materials Research Society of India (MRSI) during November 6-8, 2019. This biennial international conference had participation from 10 international delegates and about 100 delegates from national research institutes and universities from various parts of India. Considering the role played by energetic ions in nanostructuring and development of nano materials, the ICNIB 2019 provided an engaging platform for scientists and engineers to discuss a host of topics involving radiation damage, ion beam induced synthesis and modification of nanostructures, ion-beam processing of novel compound phases, nanoscale precipitates and ripple formation. Preceding the conference, a two day school to expose early researchers and research scholars to ion solid interactions, defect production, defect characterization and multi-scale modelling was organized during November 4-5, 2019.

The conference was inaugurated by Prof. Avinash Chandra Pandey, Director IUAC, New Delhi. In his inaugural lecture he presented an extensive overview of accelerators in India and their applications. In his welcome address, Dr. G. Amarendra, the then Director MSG & MMG, IGCAR stressed on the accelerator based research programme of simulating radiation damage in nuclear materials, being pursued at IGCAR. Dr. B. K. Panigrahi, Director, MC&MFCG & EIG, IGCAR presented a glimpse of past and current accelerator based research activities in IGCAR using low to medium energy ion accelerators. Awards were distributed to students who made the best poster and oral presentations.

*Reported by  
Dr. C. David, Convener, ICNIB-2019*

## Conference and Meeting Highlights

### 4th National Conference URJAVARAN – 2019

December 20, 2019



Shri Biswanath Sen, Convener, Dr. B. Venkatraman, Director, SQRMG & ESG, Shri M. Srinivas, Station Director, MAPS, Shri C. Subramaniam, Past President, ISHRAE HQ and Shri N. S. Gopala Krishna, Organizing secretary during release of souvenir in the inaugural function

4th National Conference URJAVARAN was organized by IGCAR in association with Indian Society of Heating Refrigerating & Air-conditioning Engineers (ISHRAE) - Kalpakkam Chapter at Sarabhai Auditorium, IGCAR on December 20, 2019. The theme of the conference was “Energy Sustainability Roadmap for Hospitality and Healthcare Facility”.

In the inaugural function, Shri Biswanath Sen, Convener, URJAVARAN – 2019 delivered welcome address, briefed about the conference and its impact on the society. He also presented a brief note about history of URJAVARAN. The inaugural function was presided over by Dr. B. Venkatraman, Distinguished Scientist and Director, SQRMG & ESG. In his address, Dr. B. Venkatraman emphasized the importance of indoor air quality in all buildings including health care facilities. He also indicated the necessity of reducing the huge energy consumption by heating, ventilation and air conditioning (HVAC) systems through innovative techniques thereby improving the efficiency. Shri M. Srinivas, Station Director, MAPS delivered the inaugural address and highlighted the significance of energy conservation for sustainable environment. He also emphasized on green and clean energy generation and role of DAE towards it. Shri C. Subramaniam, Past President, ISHRAE Headquarters delivered the keynote address on the topic “Building management systems, IoT & data analytics for MEP systems” and enlightened the audience about intelligent buildings and the role of building related data collection and its analysis towards optimizing the performance and improving sustainability. Shri N. S. Gopala Krishna, Organizing Secretary, URJAVARAN - 2019 proposed the vote of thanks. Shri A. Jyothish Kumar, Director (Operations), BHAVINI inaugurated the exhibition stalls at the venue of the conference. Various industries in the field of HVAC system and component design showcased their products.

About two hundred and sixty five delegates from DAE units at Kalpakkam, academic institutions, industries and leading consultants attended the conference. The main focus of the discussion was on products, latest technologies, and ongoing research in buildings with sustainable energy. The conference included invited talks by eminent speakers from academic institutions, industries, R&D organizations and leading consultants in the areas of air-conditioning & infection control of healthcare facilities, indoor air quality of buildings and high performance computing facility. Contributed papers from IGCAR and BARCF, covering wide spectra such as thermal energy storage by Nanotechnology, development of heat load estimation software, cooling tower performance, nuclear ventilation and energy conservation by implementing latest technology, were presented in the conference. The conference facilitated active interactions and exchange of ideas among delegates and experts in the area of HVAC.

During the valedictory function, Shri Faizan Ullah Khan, Convener, Technical Committee, URJAVARAN-2019 summed up the technical content of one-day conference. Dr. K. Ananthasivan, Director, RpG delivered the valedictory address. In his address he described how the air quality is degraded with industrial growth over time and its impact on human life. He emphasized the importance of technologies to improve air quality and sustainability. Shri Biswanath Sen, Convener, URJAVARAN – 2019 proposed the vote of thanks.

*Reported by*

*Shri Biswanath Sen, Convener, URJAVARAN – 2019*

## HBNI-IGCAR Corner

### Ph.D Thesis Defense

Name	Title	Date	Discipline
Shri Gurudas Pakhui	Electrochemical and Thermodynamic Investigations on Th <sup>4+</sup> and Cd-Th Alloys in LiCl-KCl Eutectic Melt	04-12-2019	Chemical Sciences
Ms. E. Jayanthi	Studies on Noble Metal Electrocatalysts Coated Diffusion Electrodes for Applications in PEM Based Sensors and Fuel Cells	17-12-2019	Chemical Sciences
Shri Chiranjit Poddar	Electrochemical and Corrosion Behavior of Ni-based Amorphous Alloys and Coatings for Nitric Acid Application	19-12-2019	Chemical Sciences
Shri Manmath Kumar Dash	Study of Microstructure and Microtexture during Thermo-mechanical Processing in Advanced Steels using Experimental and Computational Methods	01-10-2019	Engineering Sciences
Shri Aditya Narayana Singh	Study of Deformation and Fracture Behaviour of Alloy 617	29-11-2019	Engineering Sciences
Shri Shivang Tripathi	Study of SiC-based Neutron Detector for Applications in the Harsh Environment of Fast Reactors	26-12-2019	Engineering Sciences
Shri Santanu Kumar Parida	Localized Optical and Electrical Properties of III-V Nitride Nanostructures	14-10-2019	Physical Sciences
Shri P. Jegadeesan	Radiation Effects in Ceramic Oxides used in Nuclear Applications	05-11-2019	Physical Sciences
Shri Uttiyo Arnab Saha	A Study on the Metrics of Neutron Induced Primary Radiation Damage in Structural Materials using the Recent Basic Evaluated Nuclear Data Libraries	22-11-2019	Physical Sciences
Shri Renjith Ramachanadran	Study of Irradiation Effects in Reduced Activation Ferritic/Martensitic Steel and Fe <sub>9</sub> Cr Model Alloy using Positron Annihilation Spectroscopic Techniques	26-11-2019	Physical Sciences

### Awards and Honours

Near-field Optical Properties of InN Nanostructures

**Dr. Kishore Kumar Madapu**

64<sup>th</sup> DAE Solid State Physics Symposium, IIT Jodhpur, December 18-22, 2019

**Best Ph.D Thesis**

**Shri Binaya Kumar Sahoo** received Distinguished Student Award of American Physical Society - Forum on International Physics (APS-FIP) 2019

## Awards and Honours

Scientific Information Resource Division, SQRMG, IGCAR was awarded **Digitally Transformed Research Library - 2019** by Wiley for the excellence in Digital Library Technologies and User Centric Services during Wiley Library Awards, New Delhi, December 16, 2019

**N. Sreevidya** MDTD, MMG, Prize in **Metallography** contest in the category of SEM during NMD-ATM organized by Indian Institute of Metals, November 13-16, 2019, Thiruvananthapuram

## Best Paper/Poster Awards

5<sup>th</sup> International Conference on Nanostructuring by Ion Beam (ICNIB 2019), IGCAR, Kalpakkam, November 6 - 8, 2019

**Effect of Sb Ion Implantation in Bi<sub>2</sub>Se<sub>3</sub> Topological Single Crystal**

**A. Edward Prabu, S. Abhirami, R. Rajitha, P. Magudapathy, S. Amirthapandian, C. David and Awadhesh Mani**  
Best Poster Award

64<sup>th</sup> DAE Solid State Physics Symposium, IIT Jodhpur, Rajasthan, December 18-22, 2019

**A Clue to the Large Magneto-resistance in the NbAs<sub>2</sub> Semimetal**

**V. Harimohan, A. Bharathi, P. D. Babu, R. Rajaraman and C. S. Sundar**

Best Poster Award

**Structural Disorder and Compressibility Studies of RE<sub>6</sub>UO<sub>12</sub> at Extreme Conditions of Pressure and Temperature**

**Balmukund Shukla, N. R. Sanjay Kumar, N. V. Chandra Shekar, H. Jena and S. Kalavathi**

Best Poster Award

Springer International Conference on Communication Systems and Networks (ComNet 2019), Mar Baselios College of Engineering & Technology, Kerala, December 12-13, 2019

**Challenges and Impacts of RFID Technology in a Research Library**

**V Sivasankar, E. Soundararajan and S. Rajeswari**

Best Paper Award

32<sup>nd</sup> ISMAS Symposium on Mass Spectrometry (32<sup>nd</sup> ISMAS-2019), Bhabha Atomic Research Centre (BARC), Mumbai, November 27-30, 2019

**A Novel Sample Loading Method for Precise Isotopic Ratio Measurement of Lanthanum using Thermal Ionisation Mass Spectrometry (TIMS)**

**Suranjan Bera, S. Jayalakshmi, S. Nalini, C. V. S. Brahmananda Rao, T. S. Lakshmi Narasimhan**

Best Poster Award

**Best Paper/Poster Awards**

Vaporisation Studies on LiCl(s), KCl(s) and LiCl-KCl- $UCl_3$  Ternary Salt System by Knudsen Effusion Mass Spectrometry

V. V. Trinadh, P. Manikandan, Suranjan Bera, C. V. S. Brahmananda Rao and T. S. Lakshmi Narasimhan  
Best Poster Award

Ion Mobility and Mass Spectrometric Studies on Heroin

U. K. Maity, J. Namitha, P. Manoravi, M. Joseph  
Best Poster Award

57<sup>th</sup> National Metallurgist's Day (NMD) and 73<sup>rd</sup> Annual Technical Meeting (ATM), Thiruvananthapuram, Kovalam, Kerala, November 12 - 16, 2019

Comparison of Friction Stir and A-TIG Welding Process on the Evolution of Microstructure and Mechanical Properties of 9Cr-1Mo steel to AISI 316LN Stainless Steel Weld Joint

D. Sunilkumar, S. Muthukumar, M. Vasudevan, G. Madhusudan Reddy  
Best Poster Award

Characterization of Deformation and Fracture Resistance of a Reduced Activation Ferritic Steel

B. Shashank Dutt, G. Shanthi, M. Nani Babu, A. Moitra  
Best Poster Award

Influence of Artificial Pit on Corrosion Fatigue Behaviour of 316LN SS and its Weldment

A. Poonguzhali, S. Ningshen and G. Amarendra  
Best Paper Award

2<sup>nd</sup> International Conference on Metallurgy, Materials Science and Manufacturing (IMME19), NIT, Tiruchirappalli, December 27-28, 2019

Role of Tool RPM on the Evolution of Microstructure and Hardness of the Friction Stir Dissimilar Weldment of 2.25Cr-1Mo Steel to 316LN Stainless Steel

D. Sunilkumar, Jithin Mathew, S. Muthukumar, M. Vasudevan  
Best Paper Award

Influence of Large Strain Hot Deformation on Microstructural Evolution in Alloy D9

M. Arvinth Davinci  
Best Paper Award



## Best Paper/Poster Awards

International Conference on Advanced Materials and Processes for Defence Applications, ADMAT 2019, Hyderabad, September 23, 2019

Effects of Microstructures and Cyclic Loading on Mechanical Properties of Simulated HAZS of P91 Steel Weldment

**K. Mariappan**

Best Paper Award

DST-SERB National Conference on “Recent Advances in Nanomaterials Chemistry for Sustainable Development (RANCSD), Madras Christian College, Chennai, December 12 - 13, 2019

Tamarind Fruit Pulp Based Green Corrosion Inhibitor for Mild Steel in Acidic Environment

**Sangeetha Jayakumar, T. Nandakumar, M. Vadivel, C. Thinaharan, Rani P. George and John Philip**

Best Paper Award

International Conference on Recent Advances in Nanoscience and Nanotechnology, (ICRAN 2019), December 11 – 12, 2019, Stella Maris College, Chennai

Synthesis of Cellulose Capped  $\text{Fe}_3\text{O}_4$  Nanofluids Suitable for Application in Methylene Blue Dye Removal

**C. Anushree and John Philip**

Best Poster Award

Synthesis and Characterization of Phosphate Capped Magnetite Nanoparticles

**C. Anushree and John Philip**

Best Paper Award

15<sup>th</sup> International Conference on Modern Trends in Activation Analysis (MTAA-15), Bhabha Atomic Research Centre, Mumbai, November 17-22, 2019

Computer Program for Relative Method of Neutron Activation Analysis

**J. S. Brahmaji Rao, R. Acharya, R. Kumar**

Best Paper Award

Non-destructive Evaluation Techniques for Inspection of Components in Nuclear Applications

**C. K. Mukhopadhyay and S. Thirunavukkarasu**

Journal of Non destructive Testing & Evaluation, Volume 17 (18), 2019, pp. 26-31. Best Technical Paper in the Industrial Application Category. Award Presented by ISNT during NDE 2019, December 5, 2019.

## DAE Awards



Department of Atomic Energy has instituted annual awards for excellence in Science, Engineering and Technology in order to identify best performers in the area of Research, Technology Development and Engineering in the constituent units (other than Public Sector Undertakings and Aided Institutions). The Young Applied Scientist, Young Engineer, Young Technologist, Homi Bhabha Science and Technology Award and Scientific and Technical Excellence Award fall under this category. Group Achievement awards for recognition of major achievements by groups have also been instituted. Life-time Achievement Award is awarded to one who has made significant impact on the DAE's programmes. They are the icons for young scientists and engineers to emulate. The awards consist of a memento, citation and cash prize.

### The recipients of the Awards from IGCAR for the year 2018 were:

<b>Homi Bhabha Science and Technology Award</b>	: Dr. V. Jayaraman, MCD, MCMFCG
<b>DAE Scientific and Technical Excellence Award</b>	: Shri R. Jehadeesan, CD, EIG Dr. S. Ningshen, CS&TD, MMG Shri T. V. Prabhu, CFED, MCMFCG
<b>Young Scientist Award</b>	: Dr. Syamala Rao Polaki, SND, MSG
<b>Young Engineer Award</b>	: Shri Ashok Kumar, SMD, RDTG
<b>Young Applied Scientist/Technologist Award</b>	: Dr. V. D. Vijayanand, MDTD, MMG
<b>Meritorious Service Award</b>	: Shri P. K. Samikkannan, Recruitment, Admin.
<b>Meritorious Technical Support Award</b>	: Shri K. Rajeev, ROD, RFG Shri R. Jayavelu, RMD, RFG

### Group Achievement Awards:

Indigenous Development of Ion Mobility Spectrometer for Detection of Explosives.

Dr. B. K. Panigrahi, MC&MFCG (Group Leader)

Dr. M. Joseph, RRF, IGCAR. Shri T. Gokulakrishnan from EIG, Dr. N. Sivakumar, Retired, Shri K. Vijayakumar, Dr. R. Rajaraman, and Dr. P. Manoravi from MC&MFCG. Shri K. Suresh from MSG. Shri Manojkumar and Shri S. S. Gandhi from RC&IG-BARC

## DAE Awards

### FBTR Crossing Another Milestone-Operating at the Highest Power Level of 32 MWt

#### Shri A. Babu, RFG (Group Leader)

Shri S. Sathish, Ms. C. P. Deepa, Shri Devendra Kumar Sharma, Shri S. Sivakumar, Shri D. Samayaraj, Shri Liji Jacob, Shri J. Jaikhan, Shri V. Lakshmi Narayanan, Shri V. Sivakumar, Shri A. R. K. Paramaiah Krisna, Shri A. Neelamehan, Shri M. D. Vijay Kumar, Shri R. Giribabu, Shri Bishnu Nandan Madeli, Shri V. C. Rajesh, Shri Sthitapragyan Pattanayak, Shri V. Nithyanandan, Shri M. Prakash, Shri S. Mahadevan, Ms. Suceela, Shri S. Joy, Shri R. Sounder Rajan, Shri M. Karthikeyan, Shri J. Muthamizhventhan, Shri R. Jayavelu, Shri K. V. Suresh Kumar, Shri G. Shanmugam, Shri N. Manimaran, Shri M. Thangamani, Shri G. N. Chandrasekaran, Shri G. Muralitharan, Shri M. S. Koteeswaran, Shri K. Prakash, Shri D. Chandrasekaran, Shri P. V. Anil Kumar, Shri R. Vijay Anand, Shri Ashok D. Hanimal, Shri B. V. Chandramouli, Shri D.Visweswaran, Shri M. Neelamegam, Shri C. Mohandoss, Shri Gulam Hussain, Shri Kapil Dixit, Shri B. Balagopal, Shri A. Ravikumar, Shri K. K. Thakur, Shri S. Muthukumar, Shri M. Elumalai, Shri S. Sridhar, Shri C. Rajendran, Shri L. Anbalagan, Shri S. Anebarassane, Shri M. Vijayarman, Shri S. Haridas, Shri G. Irulandi, Shri M. Balamurugan, Shri Rajan Singh, Shri S. Dheeraj, Shri Prabhakaran, Shri P. Madan Mohan Polei, Shri S. Rajendran, Shri G. Ramalingam, Shri N. Sankaravelu, Shri C. S. Rajasekaran Nair, Shri N. Jayamoorthi, Shri S. Krishnan, Shri P. Thirumalaikumar, Shri L. Baburaj, Shri K. Rajeev, Shri M. Uthaman, Shri M. Rajendran, Shri A. Manikandan, Shri G. Thulaseedharan, Shri A. Thandavamoorthy, Shri R. Vinoth, Shri M. Mohan, Shri K. M. Mathai, Shri R. Ram Kumar, Shri D. Jayaraman, Shri G. Suresh, Shri P. Sreekumar, Shri Mohan Chowdhary, Shri V. Radhakrishnan Nair, Shri K. Ellappan, Shri P. M. Varughese, Shri K. A. Manick, Shri V. Christhuraj, Shri R. Ramesh, Shri K. R. Sekaran, Shri A. Abraham John, Shri N. Anbumani, Shri S. Vijayarangan, Shri P. Murugan, Shri A. V. Mani, Shri R. Ganesan, Shri M. Karpaga Kannan, Shri S. Gunasekaran, Shri R. Balasubramaniam, Shri P. Venkadeswaran, Shri S. Sulthan Saliheen, Shri T. Shanmugam, Shri A. Sivabalan, Shri M. Neelaikanta Pillai, Shri S. Saravanan, Shri K. G. Subramanian, Shri K.Kalyankumar, Shri R. Sekar, Shri T. Karthikeyan, Shri M. Babu, Shri S. Kanagaraju, Shri P. Samuthiram, Shri S. Gurunath, Shri P. Balamurali, Shri A. Ramamoorthy, Shri J. V. Srinivasan, Shri K. Thanigai Arasu, Shri T. Ravichandran, Shri C. Rajendran, Shri T. Arun, Shri M. Ganesan, Shri D. Vignesh Babu, Shri N. Ranjith Kumar, Shri Sonu Kumar, Shri R. Sundar, Shri I. Amir Abhas, Shri R. Vedhamanickam, Shri Suresh Mathew, Shri D. Vinoth, Shri N. Rajan, Shri R. Desingu, Shri J. Manikandan, Shri V. Sekar, Shri S. Elumalai, Shri N. Sathyanarayanan, Shri A. Nagallingam, Shri R. Sivalingam, Shri P. Sivanandham, Shri M. Jayasankar, Shri V. Velu, Shri Sakthivel, Shri G. Narayanasamy, Shri C. Kannan, Shri M. Sathish Kumar, Shri K. Gopal, Shri K. Ramesh, Shri V. Govindaraj, Shri U. Dhayalan, Shri N. Manivel, Shri M. Chittrarasu, Shri B. Y. S. Ganesh Prasad, Shri A. Udaya Sankar,

## DAE Awards

Shri D. Jaisrinivasan, Shri K. Rajesh, Shri M. Soundar, Shri N. Basavaiah, Shri R. Rathinavel, Shri V. Raj Kumar, Shri Bhukya Lakma, Shri G. Kuppan, Shri P. Thyyal Nayagi, Shri R. Vasanthi, Shri K. Bhanumurthy, Shri P. Munuswamy, Shri B. Kumuda, Shri T. V. Ravindranath, Shri V. Hariharan, Shri K. Ramachandran, Shri N. Gopalakrishnan, Shri Kalyana Rao Kuchipudi, Shri M. Muthukrishnan, Shri M. Murugesan, Shri D. Loganathan, Shri A. Mani, Ms. S. Manjula, Ms. Sheela Nambiar, Shri Sushant Maruti Patil, Shri G. Raghukumar, Shri D. Gautam, Ms. E. Radha, Shri Raghav Sharma, Shri V. Sathiamoorthy, Shri N. Sanjeevan, Shri K. Rajarathinam, Ms. Neethu Hanna Stephen, Shri K. Asokan, Shri Rajesh Chandrakanth, Shri R. Sher Singh, Shri Tanmoy Biswas, Shri B. Kadirappa, Shri K. Sasikumar, Shri T. C. Chacko, Shri S. Rama Rao, Ms. R. Premavathi, Shri M. Elango, Shri A. Lakshmanan, Shri G. Baskaran, Ms. P. Akilandeswari, Shri D. Devaraj, Shri T. Arun Kumar, Shri Dinkar Jha, Shri Abdul Mustak, Shri P. Saravanan, Shri Shobit Verma, Ms. S. Meena, Shri Satyanarayana Sahoo, Shri Immanuel Stephen, Shri B. Kumaravel, Shri Sachin Kale, Shri S. Satish Kumar, Shri R. Athisankaran, Shri K. B. Syam Kumar, Shri J. Sasikumar, Ms. T. Usha, Shri D. Ezhilan, Shri M. S. Chandrasekar, Ms. K. Vinolia, Shri S. Shanmugasundaram, Shri M. Ravi, Shri A. Murugesan, Shri Gowri Lakshmanan, Shri S. Sankilimurugan, Ms. C. Shyna, Shri A. Manjunathan, Ms. M. Devi, Shri A. Senthilkumar, Shri V. Alagudurai, Shri P. Ravi, Shri E. Ramesh, Shri P. Ragoth Kumar, Shri Ashish Jain, Shri B. Mohanarangan, Shri A. M. Kannan, Ms. Hema Ravichandran, Shri T. Kalaimagal, Ms. P. Swapna, Shri K. Dinesh, Shri Domesan, Ms. V. Jayachitra, Shri A. Arumugam, Shri Mohammed Mustafa, Shri S. A. Venkateswara Jeyaram, Shri S. Baskaran, Shri A. Suriyananarayanan, Shri S. Raja, Shri S. Sathish Kumar, Shri S. Thirunavukkarasu, Shri V. R. Naganathan, Shri G. Harish, Ms. M. Dhanya, Shri M. Muthukumarasamy from **RFG**. Shri Meikandamurthy, Shri S.Sureshkumar, Shri Sudheer Patri, Shri Mohammed Sabih, Ms. S. Narmadha from **FRTG**. Dr. R. Kumar, Shri J.S. Brahmaji Rao, Shri M. Venkatesh, Shri I. Lakshmi Gandhan, Ms. S. Annapoorani from **MC&MFCG**. Shri P. Narayana Rao, Shri D. Hensonraj, Shri P. Azhagesan, Shri Navtresh Bajpai from **SQ&RMG**. Shri K. Natesan, Shri S. D. Sajish, Dr. K. Devan, Shri Ram Kumar Maity, Dr. S. Clement Ravichandar, Shri Ravi Prakash Pandey, Shri M. Rajendra Kumar, Shri Juby Abraham, Shri G. S. Srinivasan, Shri D. Naga Sivayya, Shri T. Rajkumar, Shri Kulbir Singh, Shri V. L. Anuraj, Ms. Sadhna Singh, Shri P. Mohanraj, Shri Niraj Ganesh Jamdade, Shri S. Sundarlingom, Shri R. Suresh Kumar, Shri Sanjay Kumar Pandey, Shri K. Krishna Chaitanya from **RDG**. Shri Manoj Agarwal, Shri Syam Ravikumar from **BHAVINI**. Shri A. Venugopal Reddy, Shri C. Ashok Wali, Shri A. Harinarayana, Shri B. Ravinder, Shri Sanjoy Saha, Shri R. R. K. Raju, Shri Y. Ramachandra Murthy, Shri Khader Shareef, Shri G. S. N. Sastry, Shri N. Anjaiah, Shri Mohd. Yousufuddin from **NFC**.

## DAE Awards

Indigenous Development of Indian Advanced Fast Reactor Clad (IFAC-1) for Sodium Cooled FBRs.

Dr. Shaju K. Albert, MMG (Group Leader)

Dr. Arun Kumar Bhaduri, (Member)

Dr. G. Amarendra. (Member)

Dr. Gondesh Vara Prasad Reddy, Dr. Hemant Kumar, Shri M. Arul, Dr. V. D Vijayanand ,Shri B. Aashranth, Dr. Diptimayee Samantaray, Shri Arvinth Davinci, Dr. S. Latha, Dr. G. Sasikala, Shri M. Nandagopal, Shri V. Ganesan, Dr. Kinkar Laha, Shri Utpal Borah, Dr. S. Ravi, Dr. S. Raju, Dr. V. Thomas Paul, Dr. P. Parameswaran and Dr. Haraprasanna Tripathi from MMG. Dr. Christopher David, and Dr. S. Balaji from MSG. Shri V. Rajendran, Shri P. Karuppasamy, Shri A. Ramanathan, Shri S. Thiyagu, Shri V. Kodiarasan, and Dr. B. K. Panigrahi from EIG. Shri N. Raghu, Shri K. Krishna Chaitanya, Shri P. Azhagesan, Shri D. Hensonraj, Shri P. Narayana Rao from SQRMG. Dr. S. Clement Ravi Chander, Dr. S. Murugan, Shri Pramod Kumar Chaurasia, Shri M. Muthuganesh, Shri Rajesh Saxena, Shri R. Ramesh, Shri Manam Sambasiva Rao and Shri R. Ravikumar from RDTG. Shri Kumar Vaibhaw, Dr. Komal Kapoor, Shri K. Sunder Krishna, Dr. Pramanik, Shri J. K. Rout, Shri K. V. K. Deshpande, Shri P. K. Maity and Shri N. Harsha from NFC

Development of a Dual Ion Irradiation Platform for Studies of Radiation Response in Fission and Fusion Reactor Materials

Dr. G. Amarendra, (Group Leader)

Shri K. Suresh, Shri S. Chinnathambi, Dr. S. Balaji, Dr. Sachin Kumar Srivastava, Shri P. Magudapathy, Shri J. Navas, Shri A. Parthasarathi, Shri G. Natarajan, Dr. Christopher David, Dr. R. Govindaraj, Dr. M. Kamruddin from MSG and Dr. B. K. Panigrahi from (EIG)

## Biodiversity Basket - Avian Fauna

Black-crowned Night Heron



Black-crowned Night herons have short neck and legs. They have a strong stout black bill, ashy grey upper parts with glossy black capped crown, nape and crest. These birds breed in colonies of stick nests usually built over water.

**Editorial Committee Members:** Dr. T. S. Lakshmi Narasimhan, Dr. N. V. Chandra Shekar, Dr. C. K. Mukhopadhyay, Dr. Vidya Sundararajan, Shri A. Suriyanarayanan, Dr. C. V. S. Brahmananda Rao, Dr. V. Subramanian, Ms. R. Preetha, Shri J. Kodandaraman, Shri G. Venkat Kishore, Shri S. Kishore, Dr. N. Desigan, Shri M. Rajendra Kumar, Ms. S. Rajeswari, Shri K. Ganesan, Shri K. Varathan and Shri G. Pentaiah